Article

Combination of searches for the Higgs boson using the full CDF data set

CDF Collaboration

CLARK, Allan Geoffrey (Collab.), WU, Xin (Collab.)

Abstract

We present a combination of searches for the standard model Higgs boson using the full CDF run II data set, which corresponds to an integrated luminosity of 9.45–10.0 fb−1 collected from s√=1.96 TeV pp collisions at the Fermilab Tevatron. The searches consider Higgs boson production from gluon-gluon fusion, vector-boson fusion, and associated production with either a W or Z boson or a tt pair. Depending on the production mode, Higgs boson decays to W+W−, ZZ, bb, τ+τ−, and γγ are examined. We search for a Higgs boson with masses (mH) in the range 90–200 GeV/c2. In the absence of a signal, we expect based on combined search sensitivity to exclude at the 95% credibility level the mass regions 90

Reference

CDF Collaboration, CLARK, Allan Geoffrey (Collab.), WU, Xin (Collab.). Combination of searches for the Higgs boson using the full CDF data set. *Physical Review. D*, 2013, vol. 88, no. 05, p. 052013

DOI : 10.1103/PhysRevD.88.052013

Combination of searches for the Higgs boson using the full CDF data set

T. Aaltonen,[21] S. Amerio,[40a] D. Amidei,[32] A. Anastassov,[15,w] A. Annovi,[17] J. Antos,[12] G. Apollinari,[15] J. A. Appel,[15] T. Arisawa,[53] A. Artikov,[13] J. Asaadi,[48] W. Ashmanskas,[15] B. Auerbach,[2] A. Aurisano,[48] F. Azfar,[39] W. Badgett,[15] T. Bae,[25] A. Barbaro-Galtieri,[26] V. E. Barnes,[44] B. A. Barnett,[23] P. Barria,[42c,42a] P. Bartos,[12] M. Bauce,[40b,40a] F. Bedeschi,[42a] S. Behari,[15] G. Bellettini,[42b,42a] J. Bellinger,[55] D. Benjamin,[14] A. Beretvas,[15] A. Bhatti,[46] K. R. Bland,[5] B. Blumenfeld,[23] A. Bocci,[14] A. Bodek,[45] D. Bortoletto,[44] J. Boudreau,[43] A. Boveia,[11] L. Brigliadori,[6b,6a] C. Bromberg,[33] E. Brucken,[21] J. Budagov,[13] H. S. Budd,[45] K. Burkett,[15] G. Busetto,[40b,40a] P. Bussey,[19] P. Butti,[42b,42a] A. Buzatu,[19] A. Calamba,[10] S. Camarda,[4] M. Campanelli,[28] F. Canelli,[11,15,cc] B. Carls,[22] D. Carlsmith,[55] R. Carosi,[42a] S. Carrillo,[16,l] B. Casal,[9,j] M. Casarsa,[49a] A. Castro,[6b,6a] P. Catastini,[20] D. Cauz,[49a] V. Cavaliere,[22] M. Cavalli-Sforza,[4] A. Cerri,[26,e] L. Cerrito,[28,r] Y. C. Chen,[1] M. Chertok,[7] G. Chiarelli,[42a] G. Chlachidze,[15] K. Cho,[25] D. Chokheli,[13] M. A. Ciocci,[42c,42a] A. Clark,[18] C. Clarke,[54] M. E. Convery,[15] J. Conway,[7] M. Corbo,[15] M. Cordelli,[17] C. A. Cox,[7] D. J. Cox,[7] M. Cremonesi,[42a] D. Cruz,[48] J. Cuevas,[9,y] R. Culbertson,[15] N. d'Ascenzo,[15,v] M. Datta,[15,ee] P. De Barbaro,[45] L. Demortier,[46] M. Deninno,[6a] F. Devoto,[21] M. d'Errico,[40b,40a] A. Di Canto,[42b,42a] B. Di Ruzza,[15,p] J. R. Dittmann,[5] M. D'Onofrio,[27] S. Donati,[42b,42a] M. Dorigo,[49b,49a] A. Driutti,[49a] K. Ebina,[53] R. Edgar,[32] A. Elagin,[48] R. Erbacher,[7] S. Errede,[22] B. Esham,[22] R. Eusebi,[48] S. Farrington,[39] J. P. Fernández Ramos,[29] R. Field,[16] G. Flanagan,[15,t] R. Forrest,[7] M. Franklin,[20] J. C. Freeman,[15] H. Frisch,[11] Y. Funakoshi,[53] A. F. Garfinkel,[44] P. Garosi,[42c,42a] H. Gerberich,[22] E. Gerchtein,[15] S. Giagu,[47a] V. Giakoumopoulou,[3] K. Gibson,[43] C. M. Ginsburg,[15] N. Giokaris,[3] P. Giromini,[17] G. Giurgiu,[23] V. Glagolev,[13] D. Glenzinski,[15] M. Gold,[35] D. Goldin,[48] A. Golossanov,[15] G. Gomez,[9] G. Gomez-Ceballos,[30] M. Goncharov,[30] O. González López,[29] I. Gorelov,[35] A. T. Goshaw,[14] K. Goulianos,[46] E. Gramellini,[6a] S. Grinstein,[4] C. Grosso-Pilcher,[11] R. C. Group,[52,15] J. Guimaraes da Costa,[20] S. R. Hahn,[15] J. Y. Han,[45] F. Happacher,[17] K. Hara,[50] M. Hare,[51] R. F. Harr,[54] T. Harrington-Taber,[15,m] K. Hatakeyama,[5] C. Hays,[39] J. Heinrich,[41] M. Herndon,[55] A. Hocker,[15] Z. Hong,[48] W. Hopkins,[15,f] S. Hou,[1] R. E. Hughes,[36] U. Husemann,[56] J. Huston,[33] G. Introzzi,[42e,42a] M. Iori,[47b,47a] A. Ivanov,[7,o] E. James,[15] D. Jang,[10] B. Jayatilaka,[15] E. J. Jeon,[25] S. Jindariani,[15] M. Jones,[44] K. K. Joo,[25] S. Y. Jun,[10] T. R. Junk,[15] M. Kambeitz,[24] T. Kamon,[25,48] P. E. Karchin,[54] A. Kasmi,[5] Y. Kato,[38,n] W. Ketchum,[11,ff] J. Keung,[41] B. Kilminster,[15,cc] D. H. Kim,[25] H. S. Kim,[25] J. E. Kim,[25] M. J. Kim,[17] S. B. Kim,[25] S. H. Kim,[50] Y. K. Kim,[11] Y. J. Kim,[25] N. Kimura,[53] M. Kirby,[15] K. Knoepfel,[15] K. Kondo,[53,a] D. J. Kong,[25] J. Konigsberg,[16] A. V. Kotwal,[14] M. Kreps,[24] J. Kroll,[41] M. Kruse,[14] T. Kuhr,[24] M. Kurata,[50] A. T. Laasanen,[44] S. Lammel,[15] M. Lancaster,[28] K. Lannon,[36,x] G. Latino,[42c,42a] H. S. Lee,[25] J. S. Lee,[25] S. Leo,[42a] S. Leone,[42a] J. D. Lewis,[15] A. Limosani,[14,s] E. Lipeles,[41] H. Liu,[52] Q. Liu,[44] T. Liu,[15] S. Lockwitz,[56] A. Loginov,[56] D. Lucchesi,[40b,40a] J. Lueck,[24] P. Lujan,[26] P. Lukens,[15] G. Lungu,[46] J. Lys,[26] R. Lysak,[12,d] R. Madrak,[15] P. Maestro,[42c,42a] S. Malik,[46] G. Manca,[27,b] A. Manousakis-Katsikakis,[3] F. Margaroli,[47a] P. Marino,[42d,42a] M. Martínez,[4] K. Matera,[22] M. E. Mattson,[54] A. Mazzacane,[15] P. Mazzanti,[6a] R. McNulty,[27,i] A. Mehta,[27] P. Mehtala,[21] C. Mesropian,[46] T. Miao,[15] D. Mietlicki,[32] A. Mitra,[1] H. Miyake,[50] S. Moed,[15] N. Moggi,[6a] C. S. Moon,[15,z] R. Moore,[15,dd] M. J. Morello,[42d,42a] A. Mukherjee,[15] Th. Muller,[24] P. Murat,[15] M. Mussini,[6b,6a] J. Nachtman,[15,m] Y. Nagai,[50] J. Naganoma,[53] I. Nakano,[37] A. Napier,[51] J. Nett,[48] C. Neu,[52] T. Nigmanov,[43] L. Nodulman,[2] S. Y. Noh,[25] O. Norniella,[22] L. Oakes,[39] S. H. Oh,[14] Y. D. Oh,[25] I. Oksuzian,[52] T. Okusawa,[38] R. Orava,[21] L. Ortolan,[4] C. Pagliarone,[49a] E. Palencia,[9,e] P. Palni,[35] V. Papadimitriou,[15] W. Parker,[55] G. Pauletta,[49c,49a] M. Paulini,[10] C. Paus,[30] T. J. Phillips,[14] G. Piacentino,[42a] E. Pianori,[41] J. Pilot,[36] K. Pitts,[22] C. Plager,[8] L. Pondrom,[55] S. Poprocki,[15,f] K. Potamianos,[26] F. Prokoshin,[13,aa] A. Pranko,[26] F. Ptohos,[17,g] G. Punzi,[42b,42a] N. Ranjan,[44] I. Redondo Fernández,[29] P. Renton,[39] M. Rescigno,[47a] T. Riddick,[28] F. Rimondi,[6a,b] L. Ristori,[42a,15] A. Robson,[19] T. Rodriguez,[41] S. Rolli,[51,h] M. Ronzani,[42b,42a] R. Roser,[15] J. L. Rosner,[11] F. Ruffini,[42c,42a] A. Ruiz,[9] J. Russ,[10] V. Rusu,[15] A. Safonov,[48] W. K. Sakumoto,[45] Y. Sakurai,[53] L. Santi,[49c,49a] K. Sato,[50] V. Saveliev,[15,v] A. Savoy-Navarro,[15,z] P. Schlabach,[15] E. E. Schmidt,[15] T. Schwarz,[32] L. Scodellaro,[9] F. Scuri,[42a] S. Seidel,[35] Y. Seiya,[38] A. Semenov,[13] F. Sforza,[42b,42a] S. Z. Shalhout,[7] T. Shears,[27] P. F. Shepard,[43] M. Shimojima,[50,u] M. Shochet,[11] I. Shreyber-Tecker,[34] A. Simonenko,[13] P. Sinervo,[31] K. Sliwa,[51] J. R. Smith,[7] F. D. Snider,[15] V. Sorin,[4] H. Song,[43] M. Stancari,[15] R. St. Denis,[19] B. Stelzer,[31] O. Stelzer-Chilton,[31] D. Stentz,[15,w] J. Strologas,[35] Y. Sudo,[50] A. Sukhanov,[15] I. Suslov,[13] K. Takemasa,[50] Y. Takeuchi,[50] J. Tang,[11] M. Tecchio,[32] P. K. Teng,[1] J. Thom,[15,f] E. Thomson,[41] V. Thukral,[48] D. Toback,[48] S. Tokar,[12] K. Tollefson,[33] T. Tomura,[50] D. Tonelli,[15,e] S. Torre,[17] D. Torretta,[15] P. Totaro,[40a] M. Trovato,[42d,42a] F. Ukegawa,[50] S. Uozumi,[25] F. Vázquez,[16,l] G. Velev,[15] C. Vellidis,[15] C. Vernieri,[42d,42a] M. Vidal,[44] R. Vilar,[9] J. Vizán,[9,bb] M. Vogel,[35] G. Volpi,[17] P. Wagner,[41] R. Wallny,[8] S. M. Wang,[1] A. Warburton,[31] D. Waters,[28] W. C. Wester III,[15] D. Whiteson,[41,c] A. B. Wicklund,[2] S. Wilbur,[11] H. H. Williams,[41] J. S. Wilson,[32] P. Wilson,[15] B. L. Winer,[36] P. Wittich,[15,f] S. Wolbers,[15] H. Wolfe,[36] T. Wright,[32] X. Wu,[18]

Z. Wu,[5] K. Yamamoto,[38] D. Yamato,[38] T. Yang,[15] U. K. Yang,[11,q] Y. C. Yang,[25] W.-M. Yao,[26] G. P. Yeh,[15] K. Yi,[15,m] J. Yoh,[15] K. Yorita,[53] T. Yoshida,[38,k] G. B. Yu,[14] I. Yu,[25] A. M. Zanetti,[49a] Y. Zeng,[14] C. Zhou,[14] and S. Zucchelli[6b,6a]

(CDF Collaboration)

[1]*Institute of Physics, Academia Sinica, Taipei, Taiwan 11529, Republic of China*
[2]*Argonne National Laboratory, Argonne, Illinois 60439, USA*
[3]*University of Athens, 157 71 Athens, Greece*
[4]*Institut de Fisica d'Altes Energies, ICREA, Universitat Autonoma de Barcelona, E-08193, Bellaterra (Barcelona), Spain*
[5]*Baylor University, Waco, Texas 76798, USA*
[6a]*Istituto Nazionale di Fisica Nucleare Bologna, I-40127 Bologna, Italy*
[6b]*University of Bologna, I-40127 Bologna, Italy*
[7]*University of California, Davis, Davis, California 95616, USA*
[8]*University of California, Los Angeles, Los Angeles, California 90024, USA*
[9]*Instituto de Fisica de Cantabria, CSIC-University of Cantabria, 39005 Santander, Spain*
[10]*Carnegie Mellon University, Pittsburgh, Pennsylvania 15213, USA*
[11]*Enrico Fermi Institute, University of Chicago, Chicago, Illinois 60637, USA*
[12]*Comenius University, 842 48 Bratislava, Slovakia; Institute of Experimental Physics, 040 01 Kosice, Slovakia*
[13]*Joint Institute for Nuclear Research, RU-141980 Dubna, Russia*
[14]*Duke University, Durham, North Carolina 27708, USA*
[15]*Fermi National Accelerator Laboratory, Batavia, Illinois 60510, USA*
[16]*University of Florida, Gainesville, Florida 32611, USA*
[17]*Laboratori Nazionali di Frascati, Istituto Nazionale di Fisica Nucleare, I-00044 Frascati, Italy*
[18]*University of Geneva, CH-1211 Geneva 4, Switzerland*
[19]*Glasgow University, Glasgow G12 8QQ, United Kingdom*
[20]*Harvard University, Cambridge, Massachusetts 02138, USA*
[21]*Division of High Energy Physics, Department of Physics, University of Helsinki and Helsinki Institute of Physics, FIN-00014, Helsinki, Finland*
[22]*University of Illinois, Urbana, Illinois 61801, USA*
[23]*The Johns Hopkins University, Baltimore, Maryland 21218, USA*
[24]*Institut für Experimentelle Kernphysik, Karlsruhe Institute of Technology, D-76131 Karlsruhe, Germany*
[25]*Center for High Energy Physics: Kyungpook National University, Daegu 702-701, Korea; Seoul National University, Seoul 151-742, Korea; Sungkyunkwan University, Suwon 440-746, Korea; Korea Institute of Science and Technology Information, Daejeon 305-806, Korea; Chonnam National University, Gwangju 500-757, Korea; Chonbuk National University, Jeonju 561-756, Korea; Ewha Womans University, Seoul, 120-750, Korea*
[26]*Ernest Orlando Lawrence Berkeley National Laboratory, Berkeley, California 94720, USA*
[27]*University of Liverpool, Liverpool L69 7ZE, United Kingdom*
[28]*University College London, London WC1E 6BT, United Kingdom*
[29]*Centro de Investigaciones Energeticas Medioambientales y Tecnologicas, E-28040 Madrid, Spain*
[30]*Massachusetts Institute of Technology, Cambridge, Massachusetts 02139, USA*
[31]*Institute of Particle Physics: McGill University, Montréal, Québec H3A 2T8, Canada; Simon Fraser University, Burnaby, British Columbia V5A 1S6, Canada; University of Toronto, Toronto, Ontario M5S 1A7, Canada; and TRIUMF, Vancouver, British Columbia V6T 2A3, Canada*
[32]*University of Michigan, Ann Arbor, Michigan 48109, USA*
[33]*Michigan State University, East Lansing, Michigan 48824, USA*
[34]*Institution for Theoretical and Experimental Physics, ITEP, Moscow 117259, Russia*
[35]*University of New Mexico, Albuquerque, New Mexico 87131, USA*
[36]*The Ohio State University, Columbus, Ohio 43210, USA*
[37]*Okayama University, Okayama 700-8530, Japan*
[38]*Osaka City University, Osaka 588, Japan*
[39]*University of Oxford, Oxford OX1 3RH, United Kingdom*
[40a]*Istituto Nazionale di Fisica Nucleare, Sezione di Padova-Trento, I-35131 Padova, Italy*
[40b]*University of Padova, I-35131 Padova, Italy*
[41]*University of Pennsylvania, Philadelphia, Pennsylvania 19104, USA*
[42a]*Istituto Nazionale di Fisica Nucleare Pisa, I-56127 Pisa, Italy*
[42b]*University of Pisa, I-56127 Pisa, Italy*
[42c]*University of Siena, I-56127 Pisa, Italy*
[42d]*Scuola Normale Superiore, I-56127 Pisa, Italy*
[42e]*INFN Pavia and University of Pavia, I-27100 Pavia, Italy*

[43]University of Pittsburgh, Pittsburgh, Pennsylvania 15260, USA
[44]Purdue University, West Lafayette, Indiana 47907, USA
[45]University of Rochester, Rochester, New York 14627, USA
[46]The Rockefeller University, New York, New York 10065, USA
[47a]Istituto Nazionale di Fisica Nucleare, Sezione di Roma 1, I-00185 Roma, Italy
[47b]Sapienza Università di Roma, I-00185 Roma, Italy
[48]Texas A&M University, College Station, Texas 77843, USA
[49a]Istituto Nazionale di Fisica Nucleare Trieste/Udine, I-34127 Trieste, Italy
[49b]University of Trieste, I-34127 Trieste, Italy
[49c]University of Udine, I-33100 Udine, Italy
[50]University of Tsukuba, Tsukuba, Ibaraki 305, Japan
[51]Tufts University, Medford, Massachusetts 02155, USA
[52]University of Virginia, Charlottesville, Virginia 22906, USA
[53]Waseda University, Tokyo 169, Japan
[54]Wayne State University, Detroit, Michigan 48201, USA
[55]University of Wisconsin, Madison, Wisconsin 53706, USA
[56]Yale University, New Haven, Connecticut 06520, USA
(Received 30 January 2013; published 17 September 2013)

We present a combination of searches for the standard model Higgs boson using the full CDF run II data set, which corresponds to an integrated luminosity of 9.45–10.0 fb^{-1} collected from $\sqrt{s} = 1.96$ TeV $p\bar{p}$ collisions at the Fermilab Tevatron. The searches consider Higgs boson production from gluon-gluon fusion, vector-boson fusion, and associated production with either a W or Z boson or a $t\bar{t}$ pair. Depending on the production mode, Higgs boson decays to W^+W^-, ZZ, $b\bar{b}$, $\tau^+\tau^-$, and $\gamma\gamma$ are examined. We search for a Higgs boson with masses (m_H) in the range 90–200 GeV/c^2. In the absence of a signal, we expect based on combined search sensitivity to exclude at the 95% credibility level the mass regions $90 < m_H < 94$ GeV/c^2, $96 < m_H < 106$ GeV/c^2, and $153 < m_H < 175$ GeV/c^2. The observed exclusion regions are $90 < m_H < 102$ GeV/c^2 and $149 < m_H < 172$ GeV/c^2. A moderate excess of signal-like events relative to the background expectation at the level of 2.0 standard deviations is present in the

[a]Deceased.
[b]Visitor from Istituto Nazionale di Fisica Nucleare, Sezione di Cagliari, 09042 Monserrato (Cagliari), Italy.
[c]Visitor from University of California Irvine, Irvine, CA 92697, USA.
[d]Visitor from Institute of Physics, Academy of Sciences of the Czech Republic, 182 21, Czech Republic.
[e]Visitor from CERN, CH-1211 Geneva, Switzerland.
[f]Visitor from Cornell University, Ithaca, NY 14853, USA.
[g]Visitor from University of Cyprus, Nicosia CY-1678, Cyprus.
[h]Visitor from Office of Science, U.S. Department of Energy, Washington, DC 20585, USA.
[i]Visitor from University College Dublin, Dublin 4, Ireland.
[j]Visitor from ETH, 8092 Zürich, Switzerland.
[k]Visitor from University of Fukui, Fukui City, Fukui Prefecture, Japan 910-0017.
[l]Visitor from Universidad Iberoamericana, Lomas de Santa Fe, México, C.P. 01219, Distrito Federal.
[m]Visitor from University of Iowa, Iowa City, IA 52242, USA.
[n]Visitor from Kinki University, Higashi-Osaka City, Japan 577-8502.
[o]Visitor from Kansas State University, Manhattan, KS 66506, USA.
[p]Visitor from Brookhaven National Laboratory, Upton, NY 11973, USA.
[q]Visitor from University of Manchester, Manchester M13 9PL, United Kingdom.
[r]Visitor from Queen Mary, University of London, London, E1 4NS, United Kingdom.
[s]Visitor from University of Melbourne, Victoria 3010, Australia.
[t]Visitor from Muons, Inc., Batavia, IL 60510, USA.
[u]Visitor from Nagasaki Institute of Applied Science, Nagasaki 851-0193, Japan.
[v]Visitor from National Research Nuclear University, Moscow 115409, Russia.
[w]Visitor from Northwestern University, Evanston, IL 60208, USA.
[x]Visitor from University of Notre Dame, Notre Dame, IN 46556, USA.
[y]Visitor from Universidad de Oviedo, E-33007 Oviedo, Spain.
[z]Visitor from CNRS-IN2P3, Paris, F-75205 France.
[aa]Visitor from Universidad Tecnica Federico Santa Maria, 110v Valparaiso, Chile.
[bb]Visitor from Universite catholique de Louvain, 1348 Louvain-La-Neuve, Belgium.
[cc]Visitor from University of Zürich, 8006 Zürich, Switzerland.
[dd]Visitor from Massachusetts General Hospital and Harvard Medical School, Boston, MA 02114, USA.
[ee]Visitor from Hampton University, Hampton, VA 23668, USA.
[ff]Visitor from Los Alamos National Laboratory, Los Alamos, NM 87544, USA.

data for the $m_H = 125$ GeV/c^2 search hypothesis. We also present interpretations of the data within the context of a fermiophobic model and an alternative standard model incorporating a fourth generation of fermions. Finally, for the hypothesis of a new particle with mass 125 GeV/c^2, we constrain the coupling strengths of the new particle to $W^{\pm}$ bosons, Z bosons, and fermions.

DOI: 10.1103/PhysRevD.88.052013 PACS numbers: 13.85.Rm, 14.80.Bn

I. INTRODUCTION

Within the standard model (SM) [1] of particle physics, the mechanism of electroweak symmetry breaking [2] implies the existence of a single observable particle referred to as the Higgs boson, H. The mass of this neutral scalar is not predicted by the theoretical framework of the SM and must be measured experimentally. Similarly, Yukawa couplings between fundamental fermions and the Higgs field, which are responsible for fermion masses, are not predicted by the SM.

Precision electroweak measurements from LEP, SLC, and the Tevatron have been interpreted within the context of the SM to constrain the mass of the potential SM Higgs boson [3]. Including the most recent W boson and top-quark mass measurements from the Tevatron [4,5], the electroweak data are consistent with a Higgs boson mass smaller than 152 GeV/c^2 at the 95% confidence level, within the framework of the SM. Direct searches at LEP exclude the SM Higgs boson for masses less than 114.4 GeV/c^2 [6].

Recently, a new particle was observed in data collected from $\sqrt{s} = 7$–8 TeV pp collisions at the CERN Large Hadron Collider (LHC) by the ATLAS [7] and CMS [8] Collaborations. The reported measurements of the observed particle are consistent with the expectations for the SM Higgs boson with a mass of roughly 125 GeV/c^2. The specific final states contributing the greatest amount of significance to these observations are $\gamma\gamma$ and $ZZ \to \ell\ell\ell\ell$ [9]. Complementary evidence was also reported recently in the $b\bar{b}$ final state based on a combination of searches from the CDF and D0 experiments [10]. Precision measurements of the properties of the new particle such as its spin, parity, production rates via the different mechanisms, and decay branching ratios are necessary for identifying if the new particle is in fact the SM Higgs boson. Higgs boson searches at the Tevatron obtain most of their sensitivity from production and decay modes that are different from those of the LHC searches. Tevatron measurements therefore provide important contributions to the available constraints on several of these properties.

The SM Higgs boson production process with the largest cross section at the Tevatron is gluon fusion. Associated production with a W or Z boson (VH) is the second largest. The cross section for WH production is twice that of ZH and is about a factor of 10 smaller than gluon fusion. The Higgs boson decay branching fraction is dominated by $H \to b\bar{b}$ for the *low-mass* Higgs boson ($m_H < 135$ GeV/c^2) and by $H \to W^+W^-$ for the *high-mass* Higgs boson ($m_H > 135$ GeV/c^2). An inclusive search for the low-mass Higgs boson in the $H \to b\bar{b}$ decay channel is extremely challenging because the $b\bar{b}$ production rate through SM processes is many orders of magnitude larger than that expected from the Higgs boson production rate. Requiring the leptonic decay of the associated W or Z boson greatly improves the expected signal-to-background ratio in these channels. As a result, Higgs associated production followed by the $H \to b\bar{b}$ decay is the most promising channel in searches for the low-mass Higgs boson. For higher-mass Higgs boson searches, the $H \to W^+W^-$ decay, where leptons originate from the W boson decays, are the most sensitive. While the $H \to b\bar{b}$ and $H \to W^+W^-$ search channels provide the best sensitivity, searches made in all final states are combined to obtain the highest possible sensitivity to the SM Higgs boson.

This article presents a combination of CDF searches for the SM Higgs boson. The combined searches incorporate potential contributions from Higgs boson production via gluon fusion, production in association with a W or Z boson, vector-boson fusion production, and production in association with a top-quark pair. Higgs boson decay modes considered are $H \to W^+W^-$, $H \to ZZ$, $H \to b\bar{b}$, $H \to \tau^+\tau^-$, and $H \to \gamma\gamma$. The individual searches are performed for potential Higgs boson masses in the range from 90 to 200 GeV/c^2 using nonoverlapping data sets defined by distinct final states. For each search subchannel, SM backgrounds are estimated and validated using data events populating appropriately defined control regions. Finally, a discriminant, which is typically the output of a multivariate algorithm constructed from kinematic event variables, is used to separate a potential signal from much larger background event contributions. The multivariate algorithms are separately optimized for each Higgs boson mass hypothesis and for each analysis subchannel. Search results are combined by constructing a combined likelihood function based on the final discriminant distributions in each search subchannel, taking into account the correlations among channels. After performing the combined search over the full Higgs boson mass range, we focus on the 125 GeV/c^2 mass hypothesis, motivated by the recent ATLAS and CMS observations [7,8]. Assuming the LHC signal is present in CDF data, we constrain fermion and boson couplings to this new particle.

We additionally interpret the search results within the context of a fermiophobic Higgs model [11–14], which assumes SM couplings to the Higgs boson except in the case of fermions, for which the couplings are assumed to

vanish. In this model, gluon-fusion production is highly suppressed, while branching fractions for $H \to \gamma\gamma$, $H \to W^+W^-$, and $H \to ZZ$ are enhanced. We also consider an extension of the SM incorporating a heavy fourth generation of fermions (SM4). Within this model, gluon-fusion production is significantly enhanced [15–17].

This article is organized as follows: Section II briefly describes the CDF II detector and the data samples used for this combination; Sec. III describes the predictions for Higgs boson production and decay that are assumed throughout, as well as the Monte Carlo models used to predict the differential distributions; Sec. IV describes the search channels included in the combination; Sec. V describes the dominant sources of uncertainty in each channel and the correlations of these uncertainties between channels; Sec. VI describes the statistical methods used; Sec. VII presents results in the context of the SM; Sec. VIII presents results in the context of the fermiophobic model; Sec. IX presents results in the context of the SM4 model; Sec. X describes the measurement of fermion and boson couplings in the context of a new 125 GeV/c^2 boson; and Sec. XI summarizes the article.

II. THE CDF II DETECTOR AND THE FULL CDF DATA SET

The CDF II detector is described in detail elsewhere [18,19]. Silicon-strip tracking detectors [20] surround the interaction region and provide precision measurements of charged-particle trajectories in the range $|\eta| < 2$ [21]. A cylindrical drift chamber provides full coverage over the range $|\eta| < 1$. The tracking detectors are located within a 1.4 T superconducting solenoidal magnet with field oriented along the beam direction. The energies of individual particles and particle jets are measured in segmented electromagnetic and hadronic calorimeter modules arranged in a projective tower geometry surrounding the solenoid. Ionization chambers are located outside of the calorimeters to help identify muon candidates [22]. The Tevatron collider luminosity is measured with multicell gas Cherenkov detectors [23]. The total uncertainty on luminosity measurements is $\pm 6.0\%$, of which 4.4% originates from detector acceptance uncertainties and 4.0% is due to the uncertainty on the inelastic $p\bar{p}$ cross section [24].

All of the results combined in this article, with the exception of the $H \to \tau^+\tau^-$ search, use the full CDF run II data sample. Small variations in the luminosities reported for the different search channels reflect the application of channel-specific data-quality criteria designed to ensure proper data modeling. For example, the silicon detector is required to be operational for the $H \to b\bar{b}$ searches, for which the identification of secondary track vertices from b hadrons plays an important role, but not in the case of the $H \to \gamma\gamma$ search. The $H \to \gamma\gamma$ search makes use of the largest data set, 10 fb^{-1}, which is about 82% of the 12 fb^{-1} that was delivered by the Tevatron collider and about 99.5% of the luminosity in which the CDF detector was considered to be operational.

CDF uses a three-level online event selection system (trigger) to select beam collision events at a rate that can be written into permanent storage. The first trigger level relies on special-purpose hardware [25] to reduce the effective beam-crossing frequency of 1.7 MHz to an event rate of approximately 15 kHz. The second level uses a mixture of dedicated hardware and fast software algorithms to further reduce the event rate to roughly 1 kHz. Events satisfying level-two trigger requirements are read out of the detector and passed to an array of computers running fast versions of off-line reconstruction algorithms, which allow for third-level trigger decisions based on quantities that are nearly the same as those used in off-line analyses [26]. The final rate of events written into permanent storage is approximately 100 Hz. The basic trigger criteria for events used in these searches are the presence of high-transverse momentum (p_T) [21] leptons, clustered calorimeter energy deposits associated with partons originating from the collision (jets) [27], and large imbalances in the transverse energies (E_T) [21] of measured depositions within the calorimeter, associated with evidence for undetected neutrinos within the event ($\not\!\!E_T$) [21].

III. STANDARD MODEL HIGGS BOSON SIGNAL PREDICTIONS

In order to conduct the most sensitive Higgs boson search possible, we include contributions from all significant production modes that are expected to occur at the Tevatron. When conducting the search using multiple production modes, the predictions of the relative contributions of each mode and the uncertainties on those predictions are required. In addition, because we use multivariate analysis techniques, the predictions of the kinematic distributions for the signal model are also important. Here we provide a summary of the tools we use to make predictions for the Higgs boson signal. The theoretical uncertainties on the signal model play a significant role at higher masses where gluon fusion is the major production mode but are less important for low-mass Higgs boson searches where associated production is most important.

To predict the kinematic distributions of Higgs boson signal events, we use the PYTHIA [28] Monte Carlo program, with CTEQ5L [29] leading-order (LO) parton distribution functions (PDFs). We scale these Monte Carlo predictions to the highest-order cross section calculations available. The PYTHIA differential distributions for some important variables, such as the Higgs boson p_T and the number of associated jets, are also corrected based on higher-order calculations as described below. The $gg \to H$ production cross section is calculated at next-to-next-to leading order (NNLO) in quantum chromodynamics (QCD) with a next-to-next-to leading log (NNLL) resummation of soft gluons; the calculation also includes

two-loop electroweak effects and handling of the running b-quark mass [30,31]. The numerical values in Table I are updates [32] of the predictions in [31] with m_t set to 173.1 GeV/c^2 [5], and with a treatment of the massive top and bottom loop corrections up to next-to-leading-order (NLO) and next-to-leading-log (NLL) accuracy. For these calculations the factorization scale (μ_F) and renormalization scale (μ_R) are set to $\mu_F = \mu_R = m_H$, and the MSTW 2008 NNLO PDF set [33], as recommended by the PDF4LHC working group [34], is used. The calculations are refinements of earlier NNLO calculations of the $gg \to H$ production cross section [35–37]. Electroweak corrections were computed in Refs. [38,39]. Soft gluon resummation was introduced in the prediction of the $gg \to H$ production cross section in Ref. [40]. The $gg \to H$ production cross section depends strongly on the gluon PDF and the value of the strong interaction coupling constant corresponding to the value q of transferred momentum, $\alpha_s(q^2)$.

Analyses that consider $gg \to H$ production are either treated inclusively or are divided into categories based on the number of reconstructed jets. This division is described in Table II. For analyses that consider inclusive $gg \to H$ production we use uncertainties calculated from simultaneous variation of the factorization and renormalization scales by factors of 2. We use the prescription of the PDF4LHC working group [34] for evaluating PDF uncertainties on the inclusive production cross section. QCD scale uncertainties that affect the cross section through their impacts on the PDFs are included as a correlated part of the total scale uncertainty. The remainder of the PDF uncertainty is treated as uncorrelated with the QCD scale uncertainty.

For analyses seeking $gg \to H$ production that divide events into categories based on the number of reconstructed jets (see Table II), we follow Refs. [50,51] for evaluating the impacts of the scale uncertainties. We treat the QCD scale uncertainties obtained from the NNLL inclusive [30,31], NLO one or more jets [52], and NLO two or more jets [53] cross section calculations as uncorrelated with one another. We then obtain QCD scale uncertainties for the exclusive $gg \to H + 0$ jet, 1 jet, and 2 or more jet categories by propagating the uncertainties on the inclusive cross section predictions through the subtractions needed to predict the exclusive rates. For example, the $H + 0$ jet cross section is obtained by subtracting the cross section for production of Higgs bosons with one or more jets at NLO from the inclusive NNLL + NNLO cross section. We assign three separate, uncorrelated scale uncertainties with correlated and anticorrelated contributions among exclusive jet categories. The procedure in Ref. [52] is used to determine PDF model uncertainties. These are obtained separately for each bin of jet multiplicity and treated as 100% correlated among jet bins.

TABLE I. The production cross sections and decay branching fractions for the SM Higgs boson assumed for the combination.

m_H (GeV/c^2)	$\sigma_{gg\to H}$ (fb)	σ_{WH} (fb)	σ_{ZH} (fb)	σ_{VBF} (fb)	σ_{ttH} (fb)	Br($H \to b\bar{b}$) (%)	Br($H \to \tau^+\tau^-$) (%)	Br($H \to W^+W^-$) (%)	Br($H \to ZZ$) (%)	Br($H \to \gamma\gamma$) (%)
90	2442.3	394.7	224.0	114.8		81.2	8.41	0.21	0.04	0.123
95	2101.1	332.1	190.3	105.6		80.4	8.41	0.47	0.07	0.140
100	1821.8	281.1	162.7	97.3	8.0	79.1	8.36	1.11	0.11	0.159
105	1584.7	238.7	139.5	89.8	7.1	77.3	8.25	2.43	0.22	0.178
110	1385.0	203.7	120.2	82.8	6.2	74.5	8.03	4.82	0.44	0.197
115	1215.9	174.5	103.9	76.5	5.5	70.5	7.65	8.67	0.87	0.213
120	1072.3	150.1	90.2	70.7	4.9	64.9	7.11	14.3	1.60	0.225
125	949.3	129.5	78.5	65.3	4.3	57.8	6.37	21.6	2.67	0.230
130	842.9	112.0	68.5	60.5	3.8	49.4	5.49	30.5	4.02	0.226
135	750.8	97.2	60.0	56.0	3.3	40.4	4.52	40.3	5.51	0.214
140	670.6	84.6	52.7	51.9	2.9	31.4	3.54	50.4	6.92	0.194
145	600.6	73.7	46.3	48.0	2.6	23.1	2.62	60.3	7.96	0.168
150	539.1	64.4	40.8	44.5	2.3	15.7	1.79	69.9	8.28	0.137
155	484.0	56.2	35.9	41.3	2.0	9.18	1.06	79.6	7.36	0.100
160	432.3	48.5	31.4	38.2	1.8	3.44	0.40	90.9	4.16	0.053
165	383.7	43.6	28.4	36.0	1.6	1.19	0.14	96.0	2.22	0.023
170	344.0	38.5	25.3	33.4	1.4	0.79	0.09	96.5	2.36	0.016
175	309.7	34.0	22.5	31.0	1.3	0.61	0.07	95.8	3.23	0.012
180	279.2	30.1	20.0	28.7	1.1	0.50	0.06	93.2	6.02	0.010
185	252.1	26.9	17.9	26.9	1.0	0.39	0.05	84.4	15.0	0.008
190	228.0	24.0	16.1	25.1	0.9	0.32	0.04	78.6	20.9	0.007
195	207.2	21.4	14.4	23.3	0.8	0.27	0.03	75.7	23.9	0.006
200	189.1	19.1	13.0	21.7	0.7	0.24	0.03	74.1	25.6	0.005

TABLE II. Luminosities, explored mass ranges, and references for the various processes and final states (ℓ represents e or μ and $\tau_{\rm had}$ denotes a hadronic tau-lepton decay) for combined analyses. The generic labels "1×," "2×," "3×," and "4×" refer to separations based on lepton or photon categories.

Channel	Luminosity (fb^{-1})	m_H range (GeV/c^2)	Reference
$WH \to \ell\nu b\bar{b}$ 2-jet channels $4 \times (5\ b$-tag categories)	9.45	90–150	[41]
$WH \to \ell\nu b\bar{b}$ 3-jet channels $3 \times (2\ b$-tag categories)	9.45	90–150	[41]
$ZH \to \nu\bar{\nu}b\bar{b}$ (3 b-tag categories)	9.45	90–150	[42]
$ZH \to \ell^+\ell^- b\bar{b}$ 2-jet channels $2 \times (4\ b$-tag categories)	9.45	90–150	[43]
$ZH \to \ell^+\ell^- b\bar{b}$ 3-jet channels $2 \times (4\ b$-tag categories)	9.45	90–150	[43]
$H \to W^+W^-$ $2 \times (0$ jets) $+ 2 \times (1$ jet) $+ 1 \times (2$ or more jets) $+ 1 \times (\mathrm{low} - m_{\ell\ell})$	9.7	110–200	[44]
$H \to W^+W^-$ $(e - \tau_{\rm had}) + (\mu - \tau_{\rm had})$	9.7	130–200	[44]
$WH \to WW^+W^-$ (same-sign leptons) + (trileptons)	9.7	110–200	[44]
$WH \to WW^+W^-$ (trileptons with 1 $\tau_{\rm had}$)	9.7	110–200	[44]
$ZH \to ZW^+W^-$ (trileptons with 1 jet) + (trileptons with 2 or more jets)	9.7	110–200	[44]
$H \to ZZ$ (4 leptons)	9.7	120–200	[45]
$H \to \tau^+\tau^-$ (1 jet) + (2 or more jets)	6.0	100–150	[46]
$WH + ZH \to jjb\bar{b}$ (2 b-tag categories)	9.45	100–150	[47]
$H \to \gamma\gamma$ $1 \times (0$ jet) $+ 1 \times (1$ or more jets) $+ 3 \times$ (all jets)	10.0	100–150	[48]
$t\bar{t}H \to WWb\bar{b}b\bar{b}$ (4 jet, 5 jet, ≥ 6 jet) $\times$ (5 b-tag categories)	9.45	100–150	[49]

The scale choice affects the p_T spectrum of the Higgs boson when produced in gluon-gluon fusion, thus biasing the acceptance of the selection requirements and also the shapes of the distributions of the final discriminants. The effect of the acceptance change is included in the calculations of Refs. [52,53], as the experimental requirements are simulated in these calculations. The effects on the final discriminant shapes are obtained by reweighting the p_T spectrum of the Higgs boson production in the Monte Carlo simulations to higher-order calculations. The Monte Carlo signal simulation used is provided by the LO generator PYTHIA [28], which includes a parton shower and fragmentation and hadronization models. We reweight the Higgs boson p_T spectra in the PYTHIA Monte Carlo samples to that predicted by HQT [54] when making predictions of differential distributions of $gg \to H$ signal events. To evaluate the impact of the scale uncertainty on the differential spectra, we use the RESBOS [55] generator, apply the scale-dependent differences in the Higgs boson p_T spectrum to the HQT prediction, and propagate these to the final discriminants as a systematic uncertainty on the shape, which is included in the calculation of the limits.

We include all significant Higgs boson production modes in the $H \to W^+W^-$, $H \to ZZ$, and $H \to \gamma\gamma$ searches. Besides gluon-gluon fusion through virtual quark loops (ggH), we include Higgs boson production in association with a W or Z vector boson (VH) or with a top-antitop quark pair (ttH), and vector-boson fusion (VBF). For the $H \to b\bar{b}$ searches, we target the WH, ZH, VBF, and ttH production modes with specific searches. In addition to the leading signal production mode in each final state, we include contributions of subleading signal production mode, which lead to increased signal acceptance. The predictions for the WH and ZH cross sections are taken from Ref. [56]. This calculation starts with the NLO calculation of V2HV[57] and includes NNLO QCD contributions [58], as well as one-loop electroweak corrections [59]. A similar calculation of the WH cross section is available in Ref. [60]. The VBF cross section is computed at NNLO in QCD in Ref. [61]. Electroweak corrections to the VBF production cross section are computed with the HAWK program [62] and are small and negative (2%–3%) in the Higgs boson mass range considered here. We include these corrections in the VBF cross sections used for this result. The ttH production cross sections we use are from Ref. [63].

We use the predictions for the branching ratios of the Higgs boson decay from Refs. [51,64]. In this calculation, the partial decay widths for all Higgs boson decays except to pairs of W and Z bosons are computed with HDECAY [65], and the W and Z pair decay widths are computed with PROPHECY4F [66]. The relevant decay branching ratios are listed in Table I. The uncertainties on the predicted branching ratios from uncertainties in the charm- and bottom-quark masses, α_s, and missing higher-order effects are presented in Refs. [67,68].

IV. SEARCH CHANNELS

Individual searches typically consist of an event selection based on the topology and kinematic properties of the final state for the specific Higgs boson production and decay mode under consideration. Separation of a potential signal from the remaining background contributions is obtained in most cases by performing a fit, using the signal and background models, for a single discriminant variable that is the output of a multivariate algorithm, which

considers many kinematic event variables as its inputs. The quality of the background model prediction for the distribution of each input variable and the final discriminant is studied using orthogonal data samples carefully selected to validate the modeling of the major background components of each analysis channel. The search samples of each analysis are divided into various subchannels based on event information such as types of reconstructed leptons, jet multiplicity, and b-quark-tagging characterization criteria. A summary of the individual searches and the subchannels included within each is given in Table II. We attempt to group events with similar signal-to-background ratios within individual subchannels to optimize search sensitivities. This approach allows the inclusion of information from less sensitive event topologies without degrading the overall sensitivity (for example, events containing higher-impurity lepton types). In addition, the isolation of specific signal and background components within individual subchannels allows for further optimization of the multivariate discriminants trained for each, leading to additional gains in search sensitivity. The final multivariate discriminants are separately optimized for each Higgs boson mass hypothesis in 5 GeV$/c^2$ steps within the mass range under consideration.

A. $H \to b\bar{b}$ searches

For searches focusing on the $H \to b\bar{b}$ decay, the efficiency for identifying reconstructed jets originating from b quarks and the resolution of the invariant-mass measurement from the two b-quark jets are of primary importance. The three most sensitive searches in this decay mode utilize a recently developed multivariate b-quark-tagging algorithm (HOBIT) [69] which is based on the kinematic properties of tracks associated with displaced decay vertices and other characteristics of reconstructed jets sensitive to the flavor of the initiating parton. *Tight* and *loose* operating points are defined for this algorithm. For example, the loose operating point is found to have a b-quark-tagging efficiency of approximately 70% and an associated misidentification rate for light quarks and gluons of approximately 5%. Compared to the SECVTX [18] algorithm, the most commonly used b-quark-tagging algorithm at CDF, the new algorithm improves b-tag efficiency by roughly 20%, for operating points with equivalent misidentification (mistag) rates. The secondary channels that require b-jet identification (the all-hadronic and $t\bar{t}H \to t\bar{t}b\bar{b}$ searches) were not updated to use the HOBIT tagger and instead rely on the SECVTX and JETPROB [70] algorithms. The decay width of the Higgs boson is expected to be much smaller than the experimental dijet mass resolution, which is typically 15% of the mean reconstructed mass. The $H \to b\bar{b}$ searches are most sensitive in final states that include two jets. However, sometimes initial-state or final-state radiation can produce a third jet in the event. Including three-jet events increases signal acceptance and adds sensitivity, motivating the inclusion of these events in the $H \to b\bar{b}$ searches. Since a SM Higgs boson signal would appear as a broad enhancement in the reconstructed mass distribution of candidate b-quark-jet pairs, dedicated efforts to improve the mass resolution have been performed in each subchannel [71]. Along with improved b-jet identification and jet-energy resolution, the primary $H \to b\bar{b}$ analyses have all benefited from increased trigger acceptance by including events from many different trigger paths. In many cases, the complicated correlations between kinematic variables used in the trigger decision are modeled with a neural network using linear regression based on event kinematic properties and geometric acceptance [72].

1. $WH \to \ell\nu b\bar{b}$ search

The search focusing on the $WH \to \ell\nu b\bar{b}$ production and decay mode [41] has separate analysis channels for events with two and three reconstructed jets. Events are further separated into subchannels based on the type of reconstructed lepton and the quality of the tagging information associated with the candidate b-quark jets. In particular, separate subchannels are used for events containing a high-quality central muon or central electron candidate, a forward muon candidate, a forward electron candidate, and a looser central electron or muon candidate based on the presence of an isolated track [73,74]. The final two-lepton categories, which provide some acceptance for lower-quality electrons and single prong tau decays, are considered only in the case of two-jet events. For two-jet events, five subchannels are used associated with each lepton category based on the quality of the b-tagging information associated with each jet: two tight tags (TT), one tight and one loose tag (TL), a single tight tag (Tx), two loose tags (LL), and a single loose tag (Lx). In the case of three-jet events, only two b-tag subchannels, TT and TL, are considered since the other categories contribute negligibly to the overall search sensitivity. A Bayesian neural network is used to distinguish potential Higgs boson signal events from other background contributions.

2. $ZH \to \ell^+\ell^- b\bar{b}$ search

The search for $ZH \to \ell^+\ell^- b\bar{b}$ production and decay [43] is based on events with two isolated leptons and a minimum of two jets. A combination of triggers based on electromagnetic energy clusters and signals in the muon chambers matched to reconstructed tracks are used to select events containing $Z \to ee$ and $Z \to \mu\mu$ candidates. Some triggers based on missing transverse energy requirements are also used to select $Z \to \mu\mu$ candidates, taking advantage of the apparent imbalance in transverse energies that results from the muons depositing only a small fraction of their energies in the calorimeter. Neural networks are used to select dielectron and dimuon candidates [72]. The absence of missing energy from neutrinos allows for

improved dijet mass resolution through event-wide transverse momentum constraints. These are incorporated through corrections to the measured jet energies based on the observed $\not\!\!E_T$ using a neural-network approach. The search maintains separate analysis channels for events with two and three jets, as well as for events with dielectron and dimuon candidates. Each of the resulting four channels is further split into four subchannels (TT, TL, Tx, and LL) based on the quality of the tagging information available from the multivariate algorithm. Signal is separated from background in multiple phases. First, three networks are used to distinguish the ZH signal from each of the $t\bar{t}b$, Z + jets, and diboson backgrounds. Then, a final network further separates the signal from all backgrounds simultaneously.

3. $WH, ZH \to \not\!\!E_T b\bar{b}$ search

The search for $WH, ZH \to \not\!\!E_T b\bar{b}$ production and decay [42,75] is based on events with large $\not\!\!E_T$ and no isolated-lepton candidates. Additional background suppression techniques are applied to reduce large background contributions from multijet production processes. In particular, prior to construction of the final discriminant, a requirement on a multivariate discriminant trained specifically for separating potential signal from the multijet background is applied to the event sample. Events that do not satisfy this requirement are used to normalize the remaining multijet background contribution, which is modeled using a mistag rate function for gluon and light-quark jets measured in data and applied to the untagged jets in data events that otherwise satisfy the kinematic selection criteria. One of the inputs to this multivariate discriminant is a track-based missing-transverse-momentum calculation that discriminates against false $\not\!\!E_T$ [76]. A second, final multivariate discriminant is used to separate the potential Higgs boson signal from the remaining backgrounds, such as W + heavy flavor jets (where heavy flavor refers to jets originating from b or c quarks) and $t\bar{t}$ production. Events with two and three jets are treated as a single search channel that is subdivided into three subchannels (TT, TL, and Tx) based on the quality of tagging information from the multivariate algorithm.

4. All-hadronic search

The all-hadronic search [47] focuses on WH, ZH and VBF production contributing to the $jjb\bar{b}$ final state. We use events containing four or five reconstructed jets, at least two of which have been tagged as b-quark candidates based on information from the previously developed SECVTX [18] and JETPROB [70] algorithms. The use of these two algorithms results in two search subchannels containing events with either two SECVTX tagged jets (SS) or one SECVTX tagged jet and one JETPROB tagged jet (SJ). Large multijet background contributions are modeled from the data by applying a measured mistag probability to the non-b-tagged jets within data events that contain a single b-tagged jet but otherwise satisfy event selection requirements. The multivariate discriminants used to separate potential signal from the large background contributions are based on kinematic variable inputs including some variables developed to distinguish the reconstructed jets originating of b quarks from those of light quarks and gluons.

5. $t\bar{t}H \to t\bar{t}b\bar{b}$ search

The search for $t\bar{t}H \to t\bar{t}b\bar{b}$ production and decay [49] is based on events with one reconstructed lepton, large $\not\!\!E_T$, and four or more reconstructed jets in which at least two jets are identified as b-quark candidates based on the SECVTX [18] or JETPROB [70] algorithms. Events containing four, five, and six or more jets are analyzed as separate channels, and the events within each channel are further separated into five subchannels (SSS, SSJ, SJJ, SS, and SJ), based on the number of tagged jets and the algorithms contributing to each tag. Multivariate discriminant variables are used to separate potential signal from the dominant $t\bar{t}$ background contributions.

B. $H \to \tau^+\tau^-$ search

The search for Higgs bosons decaying to tau lepton pairs [46] incorporates potential contributions from all four production modes. The search is based on events containing one electron or muon candidate and one hadronically decaying tau-lepton candidate. To help reduce $Z/\gamma^* \to \tau^+\tau^-$ background contributions, events are also required to contain at least one reconstructed jet. Events that contain one jet and two or more jets are treated as independent search subchannels. Boosted decision trees are trained for both subchannels to separate potential signal events from those associated with each significantly contributing background production mechanism. Significant numbers of background events are removed from the samples by placing lower cuts on the outputs of each boosted decision tree. The output of the boosted decision tree trained to separate potential signal from $Z/\gamma^* \to \tau^+\tau^-$ background contributions is used as the final discriminating variable for events surviving all of the selection criteria.

C. $H \to W^+W^-$ search

In the search for Higgs bosons decaying to W boson pairs [44] the greatest sensitivity originates from Higgs bosons produced through gluon fusion; however, the signal contributions from all four production modes are included. The primary search is based on events with two oppositely charged isolated leptons and large $\not\!\!E_T$, focusing on the $H \to W^+W^- \to \ell^+\nu\ell^-\nu$ decay mode. The presence of neutrinos in the final state prevents an accurate reconstruction of the candidate Higgs boson mass, and separation of a potential signal from background contributions is based on other kinematic variables. In particular, the distribution of

angular separations between the final-state leptons produced in the decays of W^+W^- pairs is significantly different for pairs originating from a spin-zero particle, such as the Higgs boson signal, and the major backgrounds.

Events in the primary search are separated into eight subchannels based on the types of reconstructed leptons, the number of reconstructed jets, and the invariant mass of the dilepton pair. In the case of events with two electron or muon candidates, separate analysis channels are used for those events with zero, one, and two or more reconstructed jets. This separation helps to isolate potential signal contributions associated with the four signal production mechanisms as well as specific background contributions such as $t\bar{t}$ production, which is dominant for events containing two or more jets. Based on this separation, the final multivariate discriminant used for each channel is optimized, leading to a significant improvement in the overall search sensitivity.

In the case of events with zero or one reconstructed jet, separate search subchannels are used for events containing *low-purity* and *high-purity* lepton types. Events containing forward electron candidates, for example, have much higher background contributions from W + jets and $W + \gamma$ production processes where a jet or photon mimics the signature of an isolated-lepton candidate.

A separate search subchannel is used for events in which the dilepton mass is smaller than 16 GeV/c^2. The main background event contribution in this kinematic region originates from $W + \gamma$ production, and additional search sensitivity is obtained from the use of a separately trained multivariate discriminant focused on separating the potential signal from this particular background. Two additional search subchannels are used for events with one electron or muon candidate and a second, oppositely charged hadronically decaying tau-lepton candidate. These event samples contain significant background contributions from W + jets and multijet production processes, necessitating the use of independent search channels. No further separation of events based on the number of reconstructed jets is performed within these additional subchannels.

Higgs boson production in association with a W or Z boson in conjunction with the decay $H \to W^+W^-$ leads to additional potential signal events in other, more exotic final states. The signal contributions are expected to be small, but these final states contain much smaller contributions from SM background processes. Hence, the inclusion of these additional subchannels improves the overall search sensitivity. A search for $W^+H \to W^+W^+W^- \to \ell^+\nu\ell^+\nu jj$ production and decay is included through a subchannel focused on events containing two same-sign, isolated-lepton candidates and one or more reconstructed jets. Two additional subchannels are used to search for even smaller potential signal contributions from $W^+H \to W^+W^+W^- \to \ell^+\nu\ell^+\nu\ell^-\nu$ production and decay. These subchannels, one based entirely on electron and muon candidates and the other requiring exactly one hadronically decaying tau-lepton candidate, focus on events with a total of three isolated-lepton candidates. In all three subchannels, the final multivariate discriminants for separating potential signal from other background contributions incorporate multiple kinematic event variables including the observed $\not\!\!E_T$. The $\not\!\!E_T$ provides good separation against dominant background contributions with misidentified lepton candidates because of the presence of multiple neutrinos within each signal final state.

Finally, we use events with three isolated-lepton candidates to search for $ZH \to ZW^+W^- \to \ell^+\ell^-\ell^+\nu jj$ production and decay. Three-lepton events that are found to contain a same-flavor, opposite-sign lepton pair with a reconstructed mass within 10 GeV/c^2 of the Z boson mass are classified into one of two separate subchannels based on the presence of one reconstructed jet or two or more reconstructed jets. Within the second subchannel, all final-state particles from the Higgs boson production and decay are reconstructed (the transverse momentum components of the neutrino are obtained from the observed $\not\!\!E_T$) and a reconstructed Higgs boson mass is used as one of the kinematic input variables to the final multivariate discriminant.

D. $H \to ZZ$ search

The search for Higgs bosons decaying to Z boson pairs [45] is based on events with four reconstructed lepton candidates (electrons or muons). The selected events consist primarily of the background from nonresonant diboson production of Z^*/Z-boson pairs. A four-lepton invariant mass discriminant is used for separating the potential Higgs boson signal from the nonresonant ZZ background. The event $\not\!\!E_T$ is used as an additional discriminating variable to improve sensitivity to potential four-lepton event signal contributions from $ZH \to ZW^+W^- \to \ell^+\ell^-\ell^+\nu\ell^-\nu$ and $ZH \to \ell^+\ell^-\tau^+\tau^-$ production and decay.

E. $H \to \gamma\gamma$ search

The search for Higgs bosons decaying to photon pairs [48] incorporates potential signal contributions from all four Higgs production mechanisms. Photon candidates are reconstructed in both the central and forward calorimeters. Conversion ($\gamma \to e^+e^-$) candidates are also reconstructed in the central calorimeter. Four search channels based on these candidate types (central-central, central-forward, central-conversion, and forward-conversion) are formed from the inclusive diphoton event sample. In order to better optimize the most sensitive search category, central-central events are further separated into two subchannels consisting of events with zero reconstructed jets (where the majority of ggH events are expected) and one or more reconstructed jets (where the majority of VH and VBF events are expected). For these subchannels, multivariate discriminants using the reconstructed diphoton

mass and other kinematic event variables as inputs are used to separate the potential signal from the nonresonant backgrounds. In the other analysis channels, the diphoton invariant mass is used as the sole kinematic discriminant. For each Higgs boson mass hypothesis, the signal region is defined to be at least ± 2 standard deviations of the expected Higgs boson diphoton mass resolution. The width of signal windows were taken to be 12, 16, and 20 GeV$/c^2$ for mass hypotheses of 100–115, 120–135, and 140–150 GeV$/c^2$, respectively. The sideband regions around each signal search window are used to normalize background contributions within the signal region for all subchannels and to validate the background modeling of the multivariate discriminants for central-central events.

V. SYSTEMATIC UNCERTAINTIES

The Higgs boson signal production rate is expected to be small compared with the copious backgrounds produced in $p\bar{p}$ collisions at Tevatron energies. Systematic uncertainties associated with background predictions can be significant relative to expected signal rates in the highest s/b bins of the discriminant distributions. Therefore, it is expected that systematic uncertainties can have a large impact on search sensitivity. As an example, in the case of the search for a 125 GeV$/c^2$ Higgs boson the inclusion of systematic uncertainties weakens the sensitivity of the combined analysis by roughly 20%. We consider uncertainties that affect the normalizations as well as those that affect the shapes of the multivariate discriminants used in the searches. We refer to these, respectively, as *rate* and *shape* uncertainties. Some systematic uncertainties are correlated between analyses, between subchannels within an analysis, and between signal and background predictions within a subchannel. The nature of the fits that are performed requires careful evaluation of the common and independent sources of systematic uncertainty. The details of the statistical treatment of the uncertainties are described in Sec. VI.

The most important rate uncertainties in the backgrounds to the $WH \to Wb\bar{b}$ and $ZH \to Zb\bar{b}$ searches come from the W + jets and Z + jets backgrounds. These uncertainties are separated into heavy-flavor components and mistags. The mistags are calibrated using data control samples. Because these backgrounds are calibrated *in situ* in events with different selection requirements from the analysis search region, and because the differences between the predictions and the true rates may not be the same between the W + jets and Z + jets samples, the W + heavy flavor and Z + heavy flavor uncertainties are not correlated between analyses but are correlated between subchannels of a single analysis. This treatment ensures that we do not use the Z + jets searches to cross-calibrate the backgrounds in the W + jets searches and vice versa.

The uncertainties on the b-tag efficiencies for each b-jet selection requirement are evaluated both for true b jets and for mistagged jets. These uncertainties are propagated to each b-tag category. The resulting uncertainties are treated as correlated between the signal predictions and the background predictions. The uncertainties related to the b-tag efficiencies are treated as correlated between analyses that use the same b-tag algorithm. Similarly, the uncertainty on the total integrated luminosity as measured by the luminosity monitor is considered correlated among all signal and background Monte Carlo–based predictions in all analyses.

We ensure that each analysis uses the same cross section assumptions and theoretical uncertainties on the prediction for the production of diboson [77] (W^+W^-, $W^\pm Z$, and ZZ), $t\bar{t}$ [78], and s-channel and t-channel single-top-quark [79] events. The three diboson processes share common dependencies on factorization and renormalization scales and PDFs, so we correlate the uncertainties on all three production modes and correlate these uncertainties across all channels.

The jet energy scale is calibrated with experimental data using events in which a photon recoils from a jet, and events in which a leptonically decaying Z boson recoils from a jet [27]. The associated uncertainties are applied to each analysis. They change the predicted rates of events passing the respective selections, largely due to jet E_T requirements, but also distort the predicted shapes of the distributions of the final discriminant variables. Hence, the systematic uncertainty from the jet energy scale can be further constrained *in situ*. We do not, however, correlate the jet energy scale uncertainty from one analysis to another, because the analyses handle jet energies differently, and accept different fractions of quark and gluon jets in their respective backgrounds. For example, the neural-network jet energy correction technique used in the $ZH \to \ell^+\ell^- b\bar{b}$ channels may have a different response to the jet energy mismodeling from the response in the other $H \to b\bar{b}$ channels. Uncertainties due to initial-state and final-state gluon radiation are considered correlated with each other and across channels.

VI. STATISTICAL METHODS

The results of the searches in each subchannel are represented as distributions of data event counts in intervals (bins) of a final discriminant variable, which is separately optimized for each subchannel at each value of the Higgs boson mass m_H. Along with the observed data are predictions for each relevant source of background, each source of signal, and the associated uncertainties. These uncertainties affect the predicted yields of each component of signal and background, as well as the differential distributions of the components in each of the histograms. We also consider uncertainties that are uncorrelated from one bin to the next of each component of the predictions, usually coming from the limited size of Monte Carlo simulated samples. The signal-to-background ratios in most of the channels are of the order of a few percent or less. The final

discriminant histograms classify events into categories with different signal-to-background ratios. Events with higher discriminant output values populate bins with larger signal-to-background ratios.

This representation of the search results allows for the extraction of constraints on both the signal production rates in the decay modes selected and the background rates and shapes. Indeed, a major component of the sensitivity of the search stems from the ability of the data to constrain the rates and shapes of the major background sources. The multivariate discriminants sort the events based on signal purity. Typically, the low signal-to-background portions of the histograms have higher statistics and serve to constrain the background rates. The shapes of the predictions for each background provide the basis by which the background prediction is extrapolated into the signal-rich region, and the shape uncertainties parametrize the extrapolation uncertainties.

We use the search results to compute upper limits on the signal rate for SM Higgs boson production, to determine the best-fit value of the signal strength and couplings, and to compute p values for purposes of conducting a hypothesis test where the null hypothesis is that a Higgs boson signal is absent and the test hypothesis is that a SM Higgs boson is present with mass m_H. We employ both frequentist and Bayesian techniques. The upper limits on Higgs boson production and the cross section fits are based on a Bayesian calculation assuming a uniform prior probability density of the signal event rate, truncated to be nonnegative. The p values are computed with a frequentist method, although the handling of the systematic uncertainties is Bayesian. The approach is the same as in Refs. [80,81]. The likelihood function is a product over all channels of the Poisson probability of observing the data given the predictions, which depend on the values of the nuisance parameters that parametrize the systematic uncertainties. The likelihood L is shown below multiplied by the prior probability density π,

$$L(R, \vec{s}, \vec{b}, \vec{n}, \vec{\nu}) \times \pi(\vec{\nu}) = \prod_{i=1}^{N_C} \prod_{j=1}^{N_{\text{bins}}} (Rs_{ij} * b_{ij})^{n_{ij}} \frac{e^{-(Rs_{ij}+b_{ij})}}{n_{ij}!} \times \prod_{k=1}^{n_{\text{sys}}} e^{-\nu_k^2/2}, \quad (1)$$

where the first product is over the number of channels (N_C), and the second product is over histogram bins, each containing n_{ij} events. The observed number of events in bin j of channel i is n_{ij}. The SM signal prediction in bin ij is s_{ij}, summed over all production and decay modes contributing to channel i, and b_{ij} is the corresponding background prediction in that bin. The predictions s_{ij} and b_{ij} are functions of the nuisance parameters $\vec{\nu}$. A nuisance parameter ν_k may affect many signal and background predictions in a correlated way, such as the uncertainty on the luminosity; it may distort the distributions of signal and background predictions, as is the case with jet energy scales, or it may affect only one bin's prediction of one source of signal or background, as is the case with Monte Carlo statistical uncertainties. The prior probability distributions of the nuisance parameters are assumed to be independent Gaussians, and the units in which the nuisance parameters are expressed are in standard deviations (s.d.) with respect to their nominal values. The prior distributions for the nuisance parameters are truncated so that no prediction for the signal or background in any channel is negative. The factor R is a simultaneous scaling of all signal components. Thus, each combination presented here assumes that the relative ratios of the contributing Higgs boson production and decay modes are as predicted by the model under test, within their theoretical uncertainties. We therefore present separate combinations assuming the SM, and several choices of models allowing nonstandard couplings. We also present separate measurements of R for channels that are sensitive to one Higgs boson decay mode at a time.

To calculate the best-fit value of R, we assume a uniform prior probability density $\pi(R)$ for positive values of R and zero for negative values of R and integrate the likelihood function L multiplied by the prior probabilities for the nuisance parameters over the values of the nuisance parameters:

$$L'(R, \vec{s}, \vec{b}, \vec{n}) = \int L(R, \vec{s}, \vec{b}, \vec{n}, \vec{\nu})\pi(\vec{\nu})d\vec{\nu}. \quad (2)$$

The best-fit value of R, R_{fit}, is the value that maximizes the posterior probability density $L'(R)\pi(R)$. The 68% credibility interval on R is the shortest interval that contains 68% of the integral of the posterior density. We then define the 95% credibility upper limit on R, R_{95} with the following relation:

$$0.95 = \int_0^{R_{95}} L'(R)\pi(R)dR. \quad (3)$$

We compute the distribution of limits that are expected in the hypothesis that no signal is present by simulating experimental outcomes and computing R_{95} in each of them. The experimental outcomes are simulated by varying the values of the nuisance parameters within their uncertainties, propagating these to the predictions of b_{ij}, and then drawing simulated data counts from Poisson distributions with the means of the predicted backgrounds. The sensitivity is expressed by the median expected limit R_{95}^{med}. A value of $R_{95} < 1$ indicates that the specific signal hypothesis under test is excluded at the 95% credibility level.

To evaluate the significance of excess data events compared with the background prediction, we compute a p value, which is the probability to observe a result that is as signal-like or more than the observed result, assuming that no signal is truly present. A p value less than 1.35×10^{-3} is customarily identified as corresponding to a 3 s.d. excess, where the correspondence between the p value and the number of s.d. is computed using the integral of one tail

of a Gaussian distribution. We rank outcomes as more or less signal- or backgroundlike based on their $R_{\rm fit}$ values. We quote the local significance in the SM Higgs boson search at $m_H = 125$ GeV/c^2, motivated by the recent discovery by ATLAS and CMS [7,8].

VII. STANDARD MODEL INTERPRETATION

A. Diboson production

The search for the Higgs boson at the Tevatron is challenging due to large backgrounds relative to the expected signal rate. Multivariate techniques are employed to improve sensitivity and this increases the need to validate the background model predictions for rates and kinematic distributions. Over the past few years signals for low cross section SM processes have been successfully extracted in the same final states as those used for the primary Higgs boson searches. For example, the production cross section for electroweak single-top-quark production was measured both in the $\ell\nu b\bar{b}$ [81] and $\not\!\!E_T b\bar{b}$ [82] final states which provided important validation for the $WH \to \ell\nu b\bar{b}$ and WH, $ZH \to \not\!\!E_T b\bar{b}$ searches. Similarly, the background model and analysis framework of the $H \to W^+W^-$ search have been validated through successful measurement of diboson cross sections have been and published in three final states: $p\bar{p} \to W^+W^-$ cross section based on the $\ell^+\bar{\nu}\ell^-\nu$ decay mode [83], $p\bar{p} \to ZZ$ cross section based on the $\ell^+\ell^-\nu\bar{\nu}$ decay mode [84], and a measurement of the $p\bar{p} \to W^\pm Z$ cross section based on the $\ell^\pm\nu\ell^+\ell^-$ decay mode [85]. All three measurements were found to be in good agreement with NLO predictions.

The searches for $WH \to Wb\bar{b}$ and $ZH \to Zb\bar{b}$ production and decay require careful modeling of large background event contributions from W + jets and Z + jets production. We gauge the sensitivity of these searches, and evaluate the background modeling and analysis techniques applied within them, by extracting from these search channels a combined cross section measurement for WZ and ZZ production. The NLO SM cross section for VZ production times the branching fraction for $Z \to b\bar{b}$ is 0.68 ± 0.05 pb, about 6 times larger than the expected 0.12 ± 0.01 pb cross section times branching fraction of $VH \to Vb\bar{b}$ for a Higgs boson mass of 125 GeV/c^2.

This measurement is performed through a combination of the same set of search channels used for the $WH \to \ell\nu b\bar{b}$, $ZH \to \ell^+\ell^- b\bar{b}$, and WH, $ZH \to \not\!\!E_T b\bar{b}$ Higgs boson searches. The data sample, event reconstruction, modeling of signal and background processes, uncertainties, and subchannels are the same as in the Higgs boson search. However, dedicated multivariate discriminants are trained to separate event contributions of VZ production from those of the other backgrounds and any potential contributions from Higgs boson production are not considered. Figure 1 shows the background-subtracted, reconstructed dijet mass distribution obtained from the combination of all search channels. A fit to the data is used to determine the absolute normalizations for VZ signal and background contributions.

Separation of the VZ signal component within these search channels is obtained from a multivariate discriminant that incorporates the dijet invariant mass as one of its most powerful kinematic inputs. For improved visualization of the result of the VZ cross section measurement, we group event counts from all bins of the final discriminant distributions from each of the search channels with similar signal purity, s/b, and display the background-subtracted data contained within each grouping as a function of increasing s/b (Fig. 1). A fit to the data is used to determine the absolute normalization of the VZ signal contribution, indicated by the filled histogram, as well as the

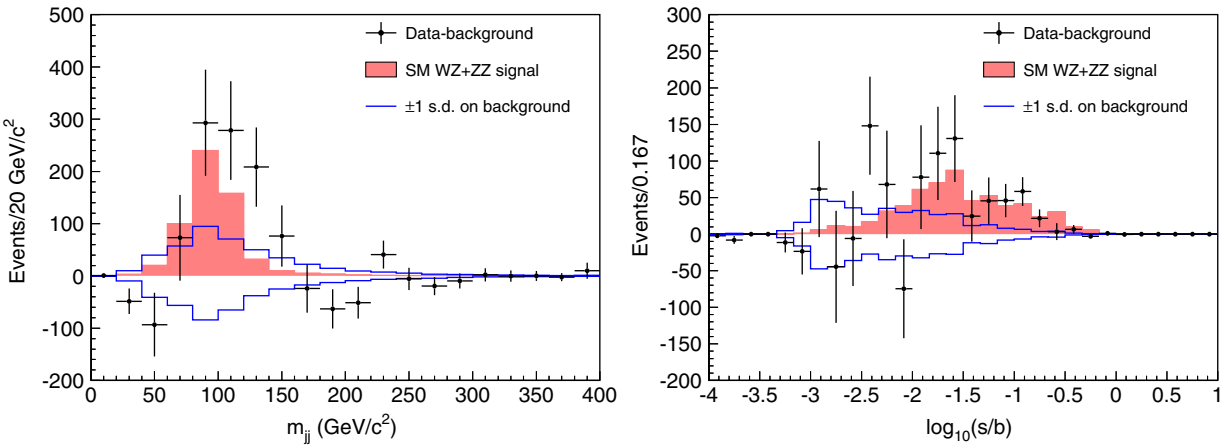

FIG. 1 (color online). Background-subtracted dijet invariant mass distribution from the combination of all search channels contributing to the VZ cross section measurement (left) and collected discriminant histograms, summing bins with similar signal-to-background ratio (s/b), for the VZ measurement (right). The expected SM signal contributions are indicated with the filled histograms. Normalizations of the subtracted background contributions, with uncertainties indicated by the unfilled histograms, are obtained from fits to the data. See Ref. [86] for alternative versions of this figure.

normalization for background contributions. The total uncertainty on the background prediction is indicated with the unfilled histogram. Based on the excess of data events in the highest s/b bins, we measure a VZ production cross section of $2.6^{+1.3}_{-1.2}$(stat + syst) pb, consistent with the SM prediction of 4.4 ± 0.3 pb [77].

B. Expected sensitivity to Higgs boson production

The median expected limit in the absence of signal, R^{med}_{95}, is shown in Fig. 2 for combinations of the search channels within each Higgs boson decay mode, and for the full combination of all channels. For Higgs boson masses below about 130 GeV/c^2, searches based on the $H \to b\bar{b}$ final state provide the greatest sensitivity. Searches based on $H \to W^+W^-$ are the most sensitive for higher Higgs boson masses. Based on the combined result we expect to exclude the regions $90 < m_H < 94$ GeV/c^2, $96 < m_H < 106$ GeV/c^2, and $153 < m_H < 175$ GeV/c^2 in the absence of signal. For the case of a Higgs boson with a mass of 125 GeV/c^2, the signal event yields, approximate mass resolutions, and median expected limits are shown in Table III for combinations of the channels associated with each Higgs boson decay mode. At this mass, $H \to b\bar{b}$ has the best sensitivity, but the $H \to W^+W^-$ searches make an important contribution to the combination.

The final sensitivities of CDF Higgs boson searches are a direct result of a substantial effort made over the last decade to significantly improve the analysis techniques used. The evolution of CDF search sensitivity over time is illustrated in Fig. 3. The points show the median expected 95% C.L. upper limits on Higgs boson production relative to SM expectations assuming the background-only

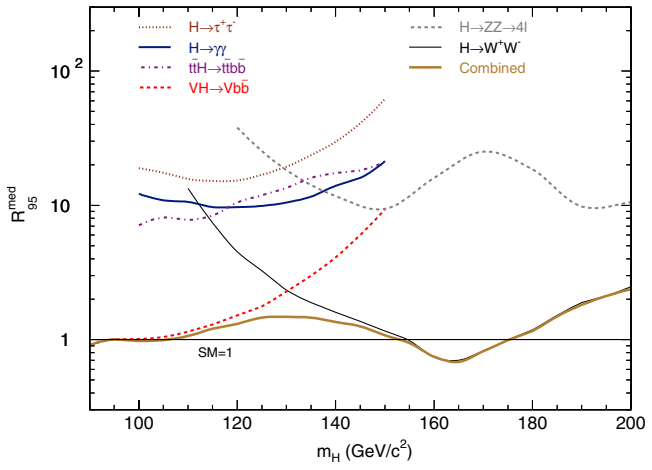

FIG. 2 (color online). Median expected 95% C.L. upper limits on Higgs boson production relative to the SM expectation assuming the background-only hypothesis for combinations of search channels within each Higgs boson decay mode and the combination of all search channels as a function of Higgs boson mass in the range between 90 and 200 GeV/c^2. See Ref. [86] for alternative versions of this figure.

TABLE III. Expected number of signal events, Higgs boson mass resolution, and median expected 95% C.L. upper limits on Higgs boson production relative to the SM expectation assuming the background-only hypothesis for combinations of search channels within each Higgs boson decay mode at $m_H = 125$ GeV/c^2.

Channel	Expected # of signal events	m_H resolution	Expected limit relative to SM
$H \to b\bar{b}$	87.0	$\approx$15%	1.77
$H \to W^+W^-$	24.2	Limited[a]	3.25
$H \to \gamma\gamma$	7.4	$\approx$2.5%	9.9
$t\bar{t}H \to WWb\bar{b}b\bar{b}$	3.6	Limited[b]	11.9
$H \to \tau^+\tau^-$	2.3	$\approx$25%	16.9
$H \to ZZ$	0.2	$\approx$3%	29

[a]Mass resolution is limited in the $H \to W^+W^-$ decay mode due to the presence of two neutrinos in the final state, which leads to an underconstrained system.
[b]Mass resolution is limited in the $t\bar{t}H \to WWb\bar{b}b\bar{b}$ production and decay mode due to the presence of four b quarks in the final state, which leads to an ambiguity in jet assignments for reconstructing the Higgs boson mass.

hypothesis from the combination of available CDF search results performed at various stages over the past decade. The integrated luminosities associated with each point are the sensitivity-weighted averages of analyzed luminosities corresponding to the analyzed samples at that time. The curves show how the sensitivity of each combination would be expected to improve in the absence of further analysis improvements assuming that sensitivity scales inversely with the square root of integrated luminosity. With respect to early versions of the CDF Higgs boson search sensitivity has been improved by more than a factor of 2 over what would be expected simply by incorporating more data. The illustrated gains in search sensitivity have originated from a wide array of analysis improvements including the inclusion of additional triggered events, improved b-jet identification algorithms, implementation of algorithms for improved jet energy resolution, inclusion of new search channels such as those considering events with additional jets, and improved multivariate techniques for separating signal and background contributions.

C. Full combination

The data are categorized into 81 subchannels for the $m_H = 125$ GeV/c^2 hypothesis. In order to better visualize the results and identify data events causing fluctuations in the observed limits and p values with respect to expectations for the background-only scenario, we perform a joint fit of the background predictions for all channels to the observed data where nuisance parameters are allowed to float within their uncertainties. We then collect bins from the final discriminant distribution by merging bins with similar s/b. The result is shown in Fig. 4, for the combined channels contributing to the searches focusing on the

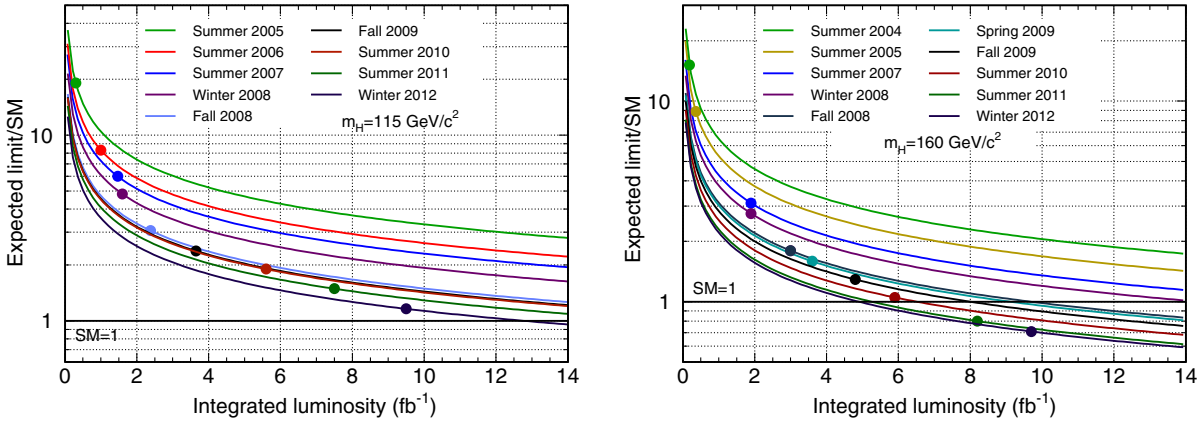

FIG. 3 (color online). Achieved and projected median expected 95% C.L. upper limits on Higgs boson production relative to the SM expectation as a function of integrated luminosity, assuming the background-only hypothesis. Each point represents a combination of CDF searches performed on the date indicated in the legend. The integrated luminosity associated with each point is the sensitivity-weighted average of the analyzed luminosities associated with each contributing channel. The solid lines show sensitivity projections, where a scaling inversely proportional to the square root of the integrated luminosity is assumed. The information is provided for combined searches performed at $m_H = 115$ GeV$/c^2$ (left) and $m_H = 160$ GeV$/c^2$ (right).

$m_H = 125$ and 165 GeV$/c^2$ mass hypotheses. The predicted Higgs boson contributions based on SM expectations summed over the bins with similar s/b are shown with the fitted background contributions overlaid. A subset of the same data is shown in Fig. 5 where the data are grouped into wider s/b bins and the backgrounds determined from the fit have been subtracted. A mild excess of data events is observed in the bins with the highest s/b for the $m_H = 125$ GeV$/c^2$ hypothesis. No such excess is seen for the case of the $m_H = 165$ GeV$/c^2$ hypothesis.

The likelihood from Eq. (1) is used to combine the Higgs boson searches from all CDF subchannels as described in Sec. VI. Figure 6 shows the resulting observed upper bound on the signal scale factor R_{95} for potential m_H values between 90 and 200 GeV$/c^2$. The median expected limit in the presence of no signal, R_{95}^{med}, is shown by the dark dashed line, while the shaded regions indicate the limit fluctuation ranges at the level of 1 and 2 standard deviations. The lighter dashed line shows the broad excess in the limits that would be expected if a SM Higgs boson with

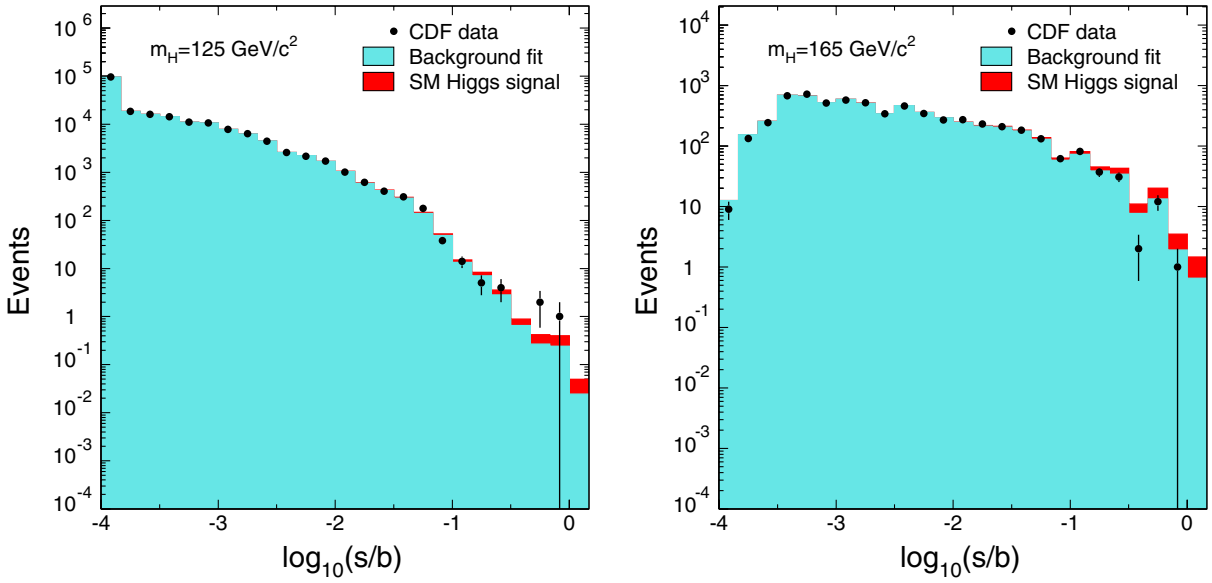

FIG. 4 (color online). Collected discriminant histograms, summed for bins with similar signal-to-background ratio (s/b), for the combined SM Higgs boson searches focusing on the $m_H = 125$ GeV$/c^2$ (left) and $m_H = 165$ GeV$/c^2$ (right) hypotheses. Normalizations of the background contributions are obtained from fits to the data. Predicted signal contributions, scaled to SM expectations, are overlaid on the backgrounds.

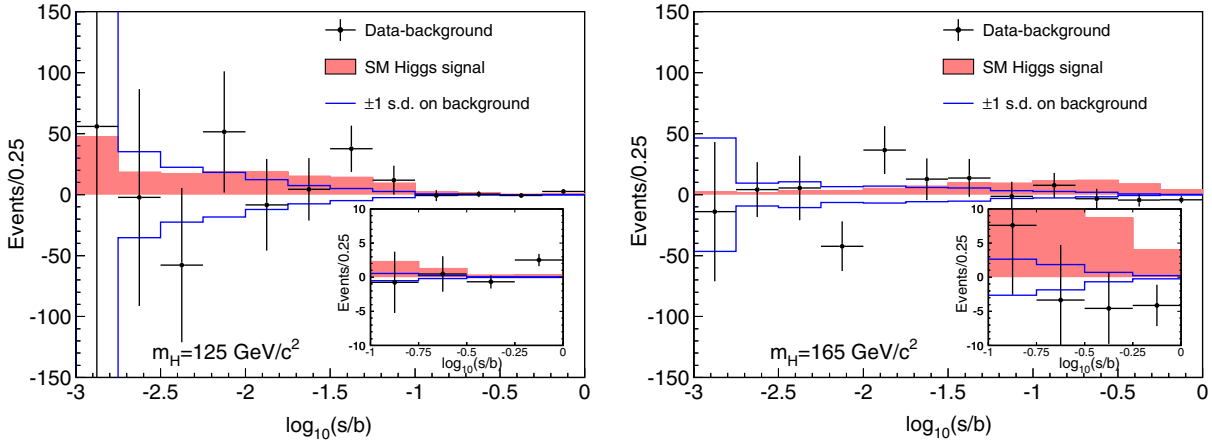

FIG. 5 (color online). Background-subtracted collected discriminant histograms, summed for bins with similar signal-to-background ratio (s/b), for the combined SM Higgs boson searches focusing on the $m_H = 125$ GeV/c^2 (left) and $m_H = 165$ GeV/c^2 (right) hypotheses. Background normalizations are obtained from fits to the data, and fit uncertainties are indicated by the unfilled histograms. Predicted signal contributions, scaled to SM expectations, are shown with the filled histograms. Uncertainties on the data points correspond to the square root of the sum of expected signal and background yields within each bin.

$m_H = 125$ GeV/c^2 were present in the data. Values of the observed and expected limits are listed in Table IV. We exclude at the 95% credibility level (C.L.) the SM Higgs boson within the mass ranges $90 < m_H < 102$ GeV/c^2 and $149 < m_H < 172$ GeV/c^2. In the absence of a signal, we expect to exclude the regions $90 < m_H < 94$ GeV/c^2, $96 < m_H < 106$ GeV/c^2, and $153 < m_H < 175$ GeV/c^2.

Mild excesses in the data compared with fitted background predictions are observed, in particular within the high s/b bins of the discriminants associated with the $WH \to \ell\nu b\bar{b}$ and $ZH \to \ell^+\ell^- b\bar{b}$ searches [41,43]. However, in the low-mass search region where there is overlap with the $H \to b\bar{b}$ searches, the $H \to W^+W^-$ search, which contributes similar search sensitivity at $m_H = 125$ GeV/c^2, does not contain data excesses in the high s/b bins of its discriminants [44]. By combining channels, the location of the data excess within the range of potential m_H values can be partially constrained based on knowledge of the available mass resolution and expected signal rates from each search channel. The constraints are observable in the measured values for $R_{\rm fit}$, which are shown as a function of m_H along with their associated 68% and 95% C.L. intervals in Fig. 7. The moderate excess is localized within the region $110 < m_H < 140$ GeV/c^2, where the measured signal rate is found to be consistent with that expected from SM Higgs boson production. The best-fit value measured for the Higgs boson production cross section at $m_H = 125$ GeV/c^2 is $1.54^{+0.77}_{-0.73}$ (stat + syst) relative to the SM prediction.

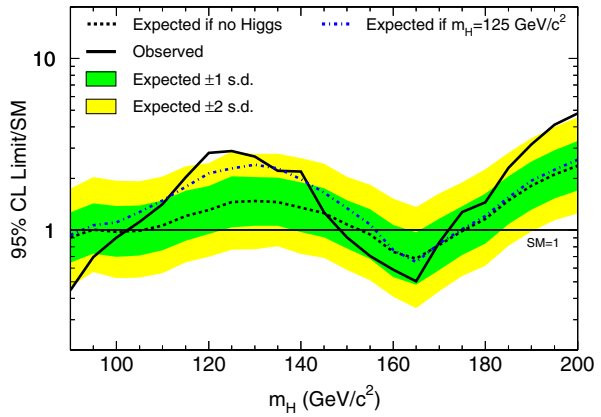

FIG. 6 (color online). Observed and expected (median, for the background-only hypothesis) 95% C.L. upper limits on SM Higgs boson production as a function of the Higgs boson mass for the combination of CDF searches. The limits are expressed as multiples of the SM prediction for test masses in 5 GeV/c^2 steps from 90 to 200 GeV/c^2. The points are connected with straight lines for improved readability. The bands indicate the 68% and 95% probability regions where the limits can fluctuate, in the absence of signal. The lighter dashed line indicates mean expected limits in the presence of a SM Higgs boson with $m_H = 125$ GeV/c^2.

The p value is shown as a function of m_H in Fig. 8. The broad excess observed in the cross section measurement is also visible in the p value. The p value for the $m_H = 125$ GeV/c^2 hypothesis is 0.0212 corresponding to a 2.0 standard deviation excess. A lower p value (0.0060) is observed for the $m_H = 120$ GeV/c^2 mass hypothesis, which is not expected to be distinguishable from the $m_H = 125$ GeV/c^2 hypothesis based on the mass resolution of the most sensitive search channels. There is also approximately a two sigma excess in our data for Higgs boson mass hypotheses above ≈ 195 GeV/c^2. Recent results from the LHC experiments strongly exclude the SM Higgs boson in this mass range [87,88]. Taking this into consideration, the mild excess near 200 GeV/c^2 is likely the result of a statistical fluctuation.

TABLE IV. Median expected (for the background-only hypothesis) and observed 95% C.L. upper limits on Higgs boson production relative to SM expectations as a function of Higgs boson mass in GeV/c^2 for the combination of CDF searches.

Mass	90	95	100	105	110	115	120	125	130	135	140	145
Expected	0.91	1.01	0.98	0.99	1.06	1.21	1.31	1.46	1.48	1.45	1.35	1.25
Observed	0.45	0.70	0.90	1.12	1.42	2.03	2.82	2.89	2.68	2.22	2.19	1.27

Mass	150	155	160	165	170	175	180	185	190	195	200
Expected	1.08	0.94	0.75	0.68	0.82	0.99	1.16	1.49	1.82	2.11	2.37
Observed	0.91	0.71	0.59	0.50	0.85	1.28	1.45	2.31	3.16	4.12	4.79

We study the couplings of a potential SM Higgs boson by also extracting best-fit signal cross sections for different combinations of channels corresponding to specific Higgs boson production and decay modes. In particular, we perform cross section fits for the subsets of CDF search channels corresponding to $VH \to Vb\bar{b}$, $H \to W^+W^-$, $H \to \gamma\gamma$, $H \to \tau^+\tau^-$, and $t\bar{t}H \to t\bar{t}b\bar{b}$ production and decay. Best-fit cross sections relative to SM expectations are provided as a function of m_H for each of these modes in Table V. A comparison of the individual mode fitted cross sections versus the fitted SM cross section obtained from all search channels is shown in Fig. 9 for the $m_H = 125$ GeV/c^2 hypothesis. The fitted signal contribution from the $H \to W^+W^-$ and $H \to \tau^+\tau^-$ channels is zero and for the $VH \to b\bar{b}$, $H \to \gamma\gamma$, and $t\bar{t}H \to t\bar{t}b\bar{b}$ channels it exceeds the SM expectation. However, all best-fit cross sections are found to be consistent within 1.5 standard deviations of SM Higgs boson expectations.

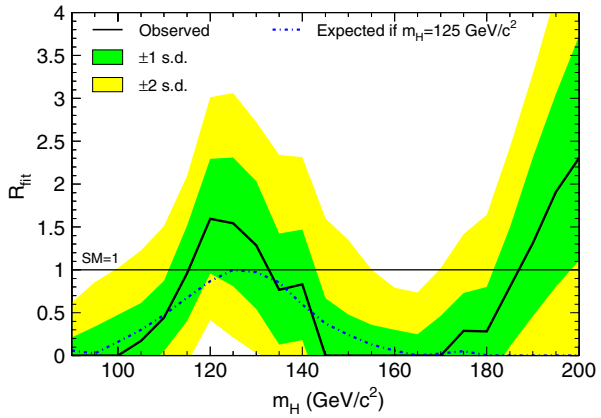

FIG. 7 (color online). Best-fit cross section for inclusive Higgs boson production, normalized to the SM expectation, for the combination of all CDF search channels as a function of the Higgs boson mass. The solid line indicates the fitted cross section, and the associated shaded regions show the 68% and 95% credibility intervals, which include both statistical and systematic uncertainties. The mean expected cross section fit values assuming the presence of a SM Higgs boson at $m_H = 125$ GeV/c^2 are shown with the dot-dashed line.

VIII. FERMIOPHOBIC MODEL INTERPRETATION

A number of theoretical models incorporate a Higgs boson with couplings to massive bosons as predicted by the SM, but negligible or zero couplings to fermions [11–14]. We denote these as fermiophobic Higgs models (FHM). Within these models $gg \to H$ production is negligible, as this mechanism is mediated at lowest order by quark loops and only higher-order weak interactions involving W and Z bosons contribute for FHM [30]. Within the FHM interpretation, production rates for WH, ZH, and VBF are assumed to be as predicted by the SM, while the production rate for $t\bar{t}H$ is assumed to be negligible. Higgs boson decay branching ratios to pairs of fermions and pairs

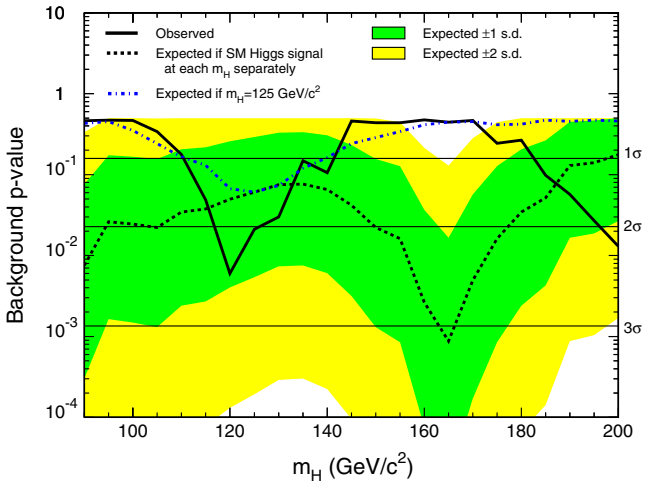

FIG. 8 (color online). The significance of the observed data excess with respect to the background-only expectation for the combination of all CDF search channels as a function of SM Higgs boson mass. The probabilities for the background model to result in a best-fit cross section as large or larger than that observed in data, p values, are shown with the solid line. The dashed line indicates the mean expected p values in the presence of a SM Higgs boson evaluated separately for each test mass, where the associated shaded regions show the ranges of 1 and 2 standard deviation fluctuations in observed p values for these scenarios. The dot-dashed line indicates mean expected p values for each mass hypothesis in the case of the SM Higgs boson with $m_H = 125$ GeV/c^2.

TABLE V. Best-fit signal cross sections, $R_{\rm fit}$, as a function of m_H for the combination of all SM search channels and for combinations of subsets of search channels corresponding to $VH \to Vb\bar{b}$, $H \to W^+W^-$, $H \to \gamma\gamma$, $H \to \tau^+\tau^-$, and $t\bar{t}H \to t\bar{t}b\bar{b}$ production and decay. The quoted uncertainties bound the smallest interval containing 68% of an integral over the posterior probability densities, which include both statistical and systematic effects.

m_H (GeV/c^2)	$R_{\rm fit}$ SM combination	$R_{\rm fit}$ $H \to W^+W^-$	$R_{\rm fit}$ $H \to b\bar{b}$	$R_{\rm fit}$ $H \to \gamma\gamma$	$R_{\rm fit}$ $H \to \tau^+\tau^-$	$R_{\rm fit}$ $t\bar{t}H \to t\bar{t}b\bar{b}$
90	$0.00^{+0.21}_{-0.00}$		$0.00^{+0.21}_{-0.00}$			
95	$0.00^{+0.34}_{-0.00}$		$0.00^{+0.34}_{-0.00}$			
100	$0.00^{+0.47}_{-0.00}$		$0.00^{+0.40}_{-0.00}$	$0.00^{+5.29}_{-0.00}$	$0.69^{+10.02}_{-0.69}$	$7.40^{+4.65}_{-3.80}$
105	$0.17^{+0.44}_{-0.17}$		$0.00^{+0.52}_{-0.00}$	$2.97^{+3.35}_{-2.97}$	$0.81^{+9.51}_{-0.81}$	$8.56^{+4.82}_{-4.10}$
110	$0.44^{+0.43}_{-0.39}$	$0.00^{+7.73}_{-0.00}$	$0.39^{+0.42}_{-0.38}$	$0.00^{+3.56}_{-0.00}$	$0.00^{+8.07}_{-0.00}$	$4.32^{+3.84}_{-3.32}$
115	$0.96^{+0.55}_{-0.55}$	$1.99^{+3.40}_{-1.99}$	$0.81^{+0.59}_{-0.52}$	$1.62^{+4.37}_{-1.62}$	$0.00^{+7.38}_{-0.00}$	$7.23^{+5.13}_{-4.56}$
120	$1.60^{+0.70}_{-0.64}$	$0.72^{+2.24}_{-0.72}$	$1.36^{+0.72}_{-0.64}$	$11.85^{+5.39}_{-4.53}$	$0.00^{+7.51}_{-0.00}$	$8.51^{+6.03}_{-5.07}$
125	$1.54^{+0.77}_{-0.73}$	$0.00^{+1.78}_{-0.00}$	$1.72^{+0.92}_{-0.87}$	$7.81^{+4.61}_{-4.42}$	$0.00^{+8.44}_{-0.00}$	$9.49^{+6.60}_{-6.28}$
130	$1.29^{+0.75}_{-0.74}$	$0.12^{+1.30}_{-0.12}$	$1.94^{+1.10}_{-1.07}$	$2.55^{+4.20}_{-2.55}$	$0.00^{+9.48}_{-0.00}$	$11.63^{+8.04}_{-6.82}$
135	$0.77^{+0.66}_{-0.64}$	$0.00^{+1.09}_{-0.00}$	$2.24^{+1.45}_{-1.33}$	$0.69^{+6.37}_{-0.69}$	$0.00^{+11.89}_{-0.00}$	$10.55^{+8.71}_{-7.15}$
140	$0.83^{+0.64}_{-0.65}$	$0.00^{+0.49}_{-0.00}$	$2.42^{+1.76}_{-1.80}$	$5.15^{+5.24}_{-4.91}$	$4.15^{+14.11}_{-4.15}$	$12.80^{+9.63}_{-8.31}$
145	$0.00^{+0.67}_{-0.00}$	$0.00^{+0.63}_{-0.00}$	$1.26^{+2.72}_{-1.26}$	$6.56^{+6.01}_{-5.72}$	$5.89^{+19.57}_{-5.89}$	$15.81^{+10.70}_{-9.29}$
150	$0.00^{+0.48}_{-0.00}$	$0.00^{+0.50}_{-0.00}$	$3.68^{+3.47}_{-3.54}$	$0.00^{+7.21}_{-0.00}$	$7.90^{+29.12}_{-7.90}$	$14.07^{+10.71}_{-9.86}$
155	$0.00^{+0.36}_{-0.00}$	$0.00^{+0.37}_{-0.00}$				
160	$0.00^{+0.30}_{-0.00}$	$0.00^{+0.29}_{-0.00}$				
165	$0.00^{+0.25}_{-0.00}$	$0.00^{+0.25}_{-0.00}$				
170	$0.00^{+0.46}_{-0.00}$	$0.00^{+0.45}_{-0.00}$				
175	$0.29^{+0.44}_{-0.29}$	$0.30^{+0.42}_{-0.30}$				
180	$0.28^{+0.52}_{-0.28}$	$0.32^{+0.52}_{-0.32}$				
185	$0.80^{+0.70}_{-0.69}$	$0.99^{+0.76}_{-0.70}$				
190	$1.31^{+1.00}_{-0.85}$	$1.55^{+1.00}_{-0.99}$				
195	$1.91^{+1.14}_{-1.11}$	$2.32^{+1.28}_{-1.15}$				
200	$2.30^{+1.42}_{-1.19}$	$3.02^{+1.55}_{-1.38}$				

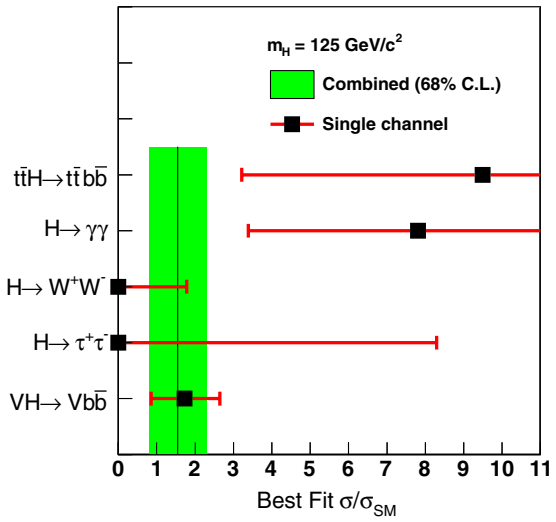

FIG. 9 (color online). Summary of best-fit signal cross sections relative to SM expectations for the $m_H = 125$ GeV/c^2 hypothesis. Square dots with horizontal uncertainty bars show the fitted cross sections obtained from the subsets of CDF search channels corresponding to $VH \to Vb\bar{b}$, $H \to W^+W^-$, $H \to \gamma\gamma$, $H \to \tau^+\tau^-$, and $t\bar{t}H \to t\bar{t}b\bar{b}$ production and decay. The solid vertical line and associated shaded region illustrate the fitted SM cross section obtained from all search channels.

of gluons are also set to zero. In addition, the decay width $\Gamma(H \to \gamma\gamma)$ is enhanced since quark-loop contributions, which subtract from the larger W-loop contribution, are absent. The complete set of decay branching ratios assumed within the FHM interpretation are listed in Table VI.

Previous searches for a fermiophobic Higgs boson at the Tevatron excluded signals with masses smaller than 119 GeV/c^2 [89–91]; the expected exclusion was also $m_{H_f} < 119\,\text{GeV}/c^2$. The ATLAS and CMS Collaborations excluded m_{H_f} in the ranges 110.0–118.0 and 119.5–121.0 GeV/c^2 using diphoton final states [92] and in the range 110–194 GeV/c^2 by combining multiple final states [93].

Dedicated searches are conducted for $H \to \gamma\gamma$ within the FHM interpretation to optimize the sensitivity for the different event kinematic properties associated with the dominant Higgs boson production mechanisms. FHM Higgs bosons are produced in association with vector bosons, or recoiling from jets in the case of VBF. As a result, the Higgs boson p_T spectrum is shifted to higher values for the FHM than the SM, where the dominant production mechanism is $gg \to H$. Potential signal contributions from WH, ZH, and VBF production included in the SM $H \to W^+W^-$ and $H \to ZZ$ search channels are

TABLE VI. Decay branching fractions of the Higgs boson in FHM computed with HDECAY [65]. Also listed are the observed 95% credibility level upper limits on the signal rate relative to FHM expectations, and the median expected limits assuming no signal is present.

m_H (GeV/c^2)	Br($\gamma\gamma$)	Br(W^+W^-)	Br(ZZ)	R_{95}^{FHM}	$R_{95,\mathrm{exp}}^{\mathrm{FHM}}$
100	0.185	0.735	0.0762	0.25	0.19
105	0.104	0.816	0.0733	0.49	0.35
110	0.0603	0.853	0.0788	0.53	0.54
115	0.0366	0.866	0.0887	1.27	0.78
120	0.0233	0.869	0.0993	1.56	0.91
125	0.0156	0.868	0.109	1.57	1.11
130	0.0107	0.867	0.116	1.32	1.22
135	7.59×10^{-3}	0.866	0.120	1.74	1.34
140	5.44×10^{-3}	0.868	0.121	2.17	1.43
145	3.90×10^{-3}	0.874	0.118	1.89	1.51
150	2.73×10^{-3}	0.886	0.108	2.33	1.57
155	1.76×10^{-3}	0.909	0.0871	1.52	1.62
160	8.35×10^{-4}	0.951	0.0466	1.53	1.51
165	3.34×10^{-4}	0.975	0.0236	1.26	1.48
170	2.26×10^{-4}	0.975	0.0246	1.95	1.73
175	1.79×10^{-4}	0.966	0.0332	2.36	1.92
180	1.48×10^{-4}	0.939	0.0609	2.92	2.23
185	1.18×10^{-4}	0.848	0.152	3.66	2.63
190	9.79×10^{-5}	0.788	0.212	4.13	3.17
195	8.52×10^{-5}	0.759	0.241	5.11	3.47
200	7.59×10^{-5}	0.742	0.258	6.02	3.80

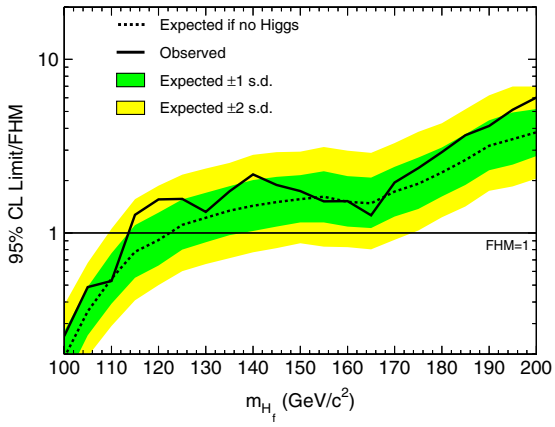

FIG. 10 (color online). Observed and expected (median, for the background-only hypothesis) 95% C.L. upper limits on Higgs boson production within the FHM interpretation as a function of Higgs boson mass. The limits are expressed as a multiple of the expected rate in the FHM for hypothesized test masses in 5 GeV/c^2 increments between 100 and 200 GeV/c^2. The individual points are joined together by straight lines for better readability. The shaded bands indicate the 68% and 95% probability regions in which the limits are expected to fluctuate in the absence of signal.

also incorporated. In the $H \to W^+W^-$ search subchannel focusing on events with opposite-charge leptons and two or more reconstructed jets, where potential signal contributions from these production mechanisms are significant, the final discriminant used for the FHM interpretation has been reoptimized to focus on the expected event kinematic properties of the relevant signal processes. The FHM search is performed over the range $100 \leq m_H \leq 200$ GeV/c^2.

No evidence for a fermiophobic Higgs boson is found in the data, and upper limits are set on the production rate relative to the FHM expectation. These limits are shown in Fig. 10 and listed in Table VI. We exclude a fermiophobic Higgs boson in the mass range $100 < m_H < 113$ GeV/c^2 and expect to exclude $100 < m_H < 122$ GeV/c^2 in the absence of a Higgs boson signal.

IX. FOURTH-GENERATION MODEL INTERPRETATION AND MODEL-INDEPENDENT LIMIT ON $gg \to H$ PRODUCTION

The lowest-order process mediating the ggH coupling in the SM is a quark triangle loop, with the dominant contribution coming from the top quark and a smaller contribution from the bottom quark. The model tested here is the standard model with a fourth sequential generation of fermions (SM4). The masses of the components of the fourth generation are assumed to be larger than the mass bounds from collider experiments. In the SM4, the up-type (u_4) and down-type (d_4) quarks would contribute approximately with the same magnitude as the top quark to the ggH coupling, resulting in approximately a factor of 9 increase in the $gg \to H$ production cross section and the $H \to gg$ decay width [15–17]. The enhancement is modified by resonant structure in the quark loop (the top quark contributes most strongly when $m_H \approx 2m_t$), electroweak contributions [16], and QCD radiative corrections [17]. The decay branching fractions of the Higgs boson may further be modified by the presence of a fourth neutrino (ν_4), which may have been too heavy to be discovered at LEP, or due to decays to a heavy fourth-generation charged lepton ℓ_4. We do not include acceptance for these decays in our predicted signal yields. The precision electroweak constraints that place an upper bound on the SM Higgs boson mass [15] are significantly relaxed in the SM4, allowing Higgs boson masses up to 750 GeV/c^2.

The production cross section for $gg \to H$ is computed in Ref. [17] for two scenarios of m_{u_4} and m_{d_4}, but the production rates do not depend significantly on these masses, once they are large enough to evade experimental bounds. If $2m_{\ell_4} < m_H$ and $2m_{\nu_4} < m_H$, the decay branching ratios have a large impact on our ability to test the model. In both scenarios we assume $m_{u_4} = 450$ GeV/c^2 and $m_{d_4} = 400$ GeV/c^2. In the first scenario, called the high-mass scenario, we assume $m_{\ell_4} = m_{\nu_4} = 1000$ GeV/c^2, and in the second scenario, the low-mass scenario, $m_{\ell_4} = 100$ GeV/c^2 and $m_{\nu_4} = 80$ GeV/c^2.

TABLE VII. Observed and median expected upper limits on $\sigma \times \mathrm{Br}(H \to W^+W^-)$ at the 95% C.L., as well as the predicted $gg \to H$ production cross sections and decay branching fractions in the SM4 with $m_{\nu_4} = 80$ GeV/c^2, $m_{\ell_4} = 100$ GeV/c^2, $m_{d_4} = 400$ GeV/c^2, and $m_{u_4} = 450$ GeV/c^2.

m_H	Obs	Exp	$\sigma(gg \to H)$	Low-mass scenario				High-mass scenario	
(GeV/c^2)	limit (pb)	limit (pb)	(pb)	Br(W^+W^-)	Br(ZZ)	Br($\nu_4\bar{\nu}_4$)	Br($\ell_4^+\ell_4^-$)	Br(W^+W^-)	Br(ZZ)
110	1.42	1.32	12.3	0.0283	2.62×10^{-3}	0.00	0.00	0.0283	2.62×10^{-3}
115	1.18	1.09	10.7	0.0505	5.17×10^{-3}	0.00	0.00	0.0505	5.17×10^{-3}
120	1.04	0.97	9.38	0.0834	9.52×10^{-3}	0.00	0.00	0.0834	9.52×10^{-3}
125	0.97	0.91	8.24	0.129	0.0161	0.00	0.00	0.129	0.0161
130	0.81	0.83	7.26	0.188	0.0251	0.00	0.00	0.188	0.0251
135	0.67	0.81	6.41	0.260	0.0362	0.00	0.00	0.260	0.0362
140	0.70	0.73	5.68	0.346	0.0483	0.00	0.00	0.346	0.0483
145	0.63	0.67	5.05	0.443	0.0597	0.00	0.00	0.443	0.0597
150	0.40	0.60	4.50	0.553	0.0672	0.00	0.00	0.553	0.0672
155	0.32	0.51	4.02	0.681	0.0653	0.00	0.00	0.681	0.0653
160	0.26	0.35	3.60	0.850	0.0409	0.00	0.00	0.850	0.0409
165	0.29	0.32	3.22	0.906	0.0199	0.0387	0.00	0.942	0.0207
170	0.34	0.36	2.89	0.888	0.0207	0.0672	0.00	0.952	0.0222
175	0.46	0.40	2.60	0.863	0.0279	0.0893	0.00	0.948	0.0306
180	0.53	0.43	2.35	0.828	0.0510	0.104	0.00	0.925	0.0569
185	0.61	0.46	2.12	0.742	0.138	0.107	0.00	0.831	0.154
190	0.73	0.49	1.92	0.687	0.194	0.109	0.00	0.770	0.217
195	0.90	0.50	1.74	0.661	0.217	0.112	0.00	0.745	0.244
200	0.83	0.55	1.58	0.647	0.230	0.114	0.00	0.730	0.260
210	1.13	0.53	1.31	0.620	0.239	0.115	0.0187	0.715	0.276
220	0.82	0.52	1.09	0.600	0.242	0.112	0.0393	0.708	0.284
230	0.82	0.50	0.912	0.588	0.242	0.108	0.0551	0.703	0.290
240	0.92	0.53	0.767	0.581	0.244	0.104	0.0663	0.700	0.294
250	0.76	0.44	0.649	0.577	0.245	0.0991	0.0738	0.697	0.296
260	0.57	0.40	0.551	0.575	0.247	0.0944	0.0787	0.695	0.299
270	0.54	0.37	0.470	0.575	0.250	0.0898	0.0814	0.693	0.301
280	0.50	0.32	0.403	0.576	0.252	0.0853	0.0827	0.692	0.303
290	0.53	0.31	0.347	0.577	0.255	0.0810	0.0829	0.690	0.305
300	0.41	0.27	0.300	0.579	0.258	0.0770	0.0823	0.689	0.306

We search for $gg \to H$ production primarily in the $H \to W^+W^-$ decay mode, but the $H \to ZZ$ decay mode also contributes, particularly for $m_H > 200$ GeV/c^2. The $H \to \gamma\gamma$ channels contribute in the SM mainly through the $gg \to H$ production, but this decay mode is suppressed due to negative contributions of the quark loops relative to the W-mediated loop in $H \to \gamma\gamma$ decay. We therefore include only the $H \to W^+W^-$ and $H \to ZZ \to \ell^+\ell^-\ell^+\ell^-$ searches in this interpretation.

Previous interpretations of SM Higgs boson searches within the context of a fourth generation of fermions at Tevatron excluded $131 < m_H < 207\,\mathrm{GeV}/c^2$ [94]. Searches with similar sensitivity were performed by the ATLAS [95] and CMS [96] Collaborations, excluding $140 < m_H < 185$ GeV/c^2 and $144 < m_H < 207$ GeV/c^2, respectively. A more recent search by the CMS Collaboration excluded the mass range $110 < m_H < 600$ GeV/c^2 [97].

The first step is to set a limit on $\sigma(gg \to H) \times Br(H \to W^+W^-)$, which can be interpreted in a variety of models. We assume the SM value for the ratio of $Br(H \to ZZ)/Br(H \to W^+W^-)$ when combining the ZZ results, an assumption which is accurate in the SM4. The $H \to W^+W^-$ channels are reoptimized for this search by training the discriminants to separate only the $gg \to H$ mode from the background, ignoring the WH, ZH, and VBF production modes. In setting upper limits on the $gg \to H$ production cross section, we also ignore the acceptance for WH, ZH, and VBF production, which yields conservative limits. In setting limits on $\sigma(gg \to H) \times Br(H \to W^+W^-)$, we do not include uncertainties in theoretical predictions of the production cross section or the decay branching ratio, but we include the theoretical uncertainties on the relative signal expectations in the 0-jet, 1-jet, and 2 + jet event selections in the $H \to W^+W^-$ searches. We search for Higgs bosons in the mass range $110 < m_H < 300\,\mathrm{GeV}/c^2$, in which the analysis is expected to be sensitive to the SM4. Limits on $\sigma(gg \to H) \times Br(H \to W^+W^-)$ are listed in Table VII and are shown in Fig. 11.

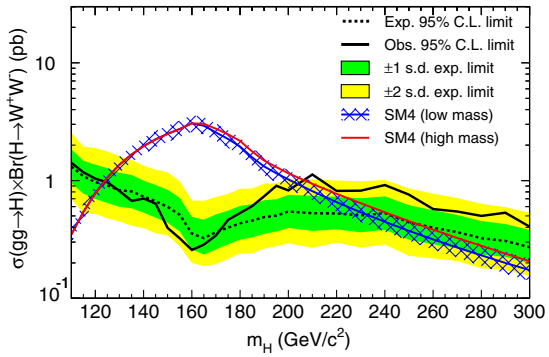

FIG. 11 (color online). Observed and expected (median, for the background-only hypothesis) 95% C.L. upper limits on the production rate for $gg \to H \to W^+W^-$ in picobarns, as functions of the Higgs boson mass. The points are joined by straight lines for better readability. The bands indicate the 68% and 95% probability regions where the limits can fluctuate, in the absence of signal. Also shown are the predictions for the two SM4 scenarios described in the text.

The second step in the SM4 interpretation is to consider specific model scenarios. In this step we reintroduce the theoretical uncertainties on the predicted cross sections due to QCD factorization and renormalization scale and PDF uncertainties. The limits obtained are shown in Fig. 12 as multiples of the predictions in the two scenarios. In the low-mass scenario, we exclude the range $124 < m_H < 203$ GeV$/c^2$ at the 95% C.L. and expect to exclude $123 < m_H < 231$ GeV$/c^2$. In the high-mass scenario, the lack of fourth-generation leptonic and neutrino decays provides more expected signal in the remaining visible decays. We exclude the range $124 < m_H < 206$ GeV$/c^2$ at the 95% C.L. and expect to exclude the range $123 < m_H < 245$ GeV$/c^2$.

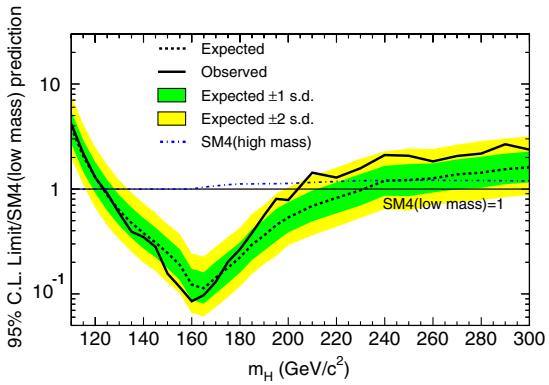

FIG. 12 (color online). Observed and expected (median, for the background-only hypothesis) 95% C.L. upper limits on Higgs boson production as a function of Higgs boson mass, in the SM4 model in the low-mass scenario, which gives the loosest mass bounds. The prediction for the high-mass scenario is also shown. The limits are expressed as a multiple of the SM4 prediction. The points are joined by straight lines for better readability. The bands indicate the 68% and 95% probability regions where the limits can fluctuate, in the absence of signal.

X. CONSTRAINTS ON FERMIONIC AND BOSONIC COUPLINGS

Following the recent LHC observations of a new Higgs-like particle with a mass of approximately 125 GeV$/c^2$, we focus on this mass hypothesis and test the couplings of the new particle, assuming that the mild observed excesses in CDF's Higgs boson searches originate from this source. Similar studies of the couplings have been performed by CMS [98] and ATLAS [99].

We assume that the production and decay of the Higgs-like particle follow the predictions of the SM Higgs boson, but with modified coupling strengths to fermions, the W boson, and the Z boson. We follow the procedures and notation of Ref. [100] and scale all Higgs boson couplings to fermions, regardless of flavor, by the factor κ_f; we scale the HWW coupling by the factor κ_W, and the HZZ coupling by the factor κ_Z. The predicted signal rates in each production and decay mode are functions of the SM predictions and the factors κ_f, κ_W, and κ_Z. The SM predictions are obtained by setting $\kappa_f = \kappa_W = \kappa_Z = 1$. Because the κ factors scale the couplings, the production rates and decay widths are quadratic functions of the coupling scale factors. The decay branching ratios are computed from the decay widths and thus are ratios of quadratic functions of the coupling scale factors.

For each of the studies described below, we assume a uniform prior probability density in one or more of the coupling scale factors and compute the posterior probability density using all of CDF SM Higgs boson search results, integrating over systematic uncertainties. One-dimensional intervals are quoted as the shortest set of intervals containing 68% of the integral of the posterior density, and the two-dimensional contours are those with the smallest areas containing 68% and 95% of the integral of the posterior density. The values that maximize the posterior probability are quoted as best-fit values.

We study both positive and negative values of the coupling scale factors, although little information on the relative signs of the couplings remains after squaring the amplitudes. The posterior probability densities have multiple maxima, possibly asymmetric due to interference terms in the production and decay in some modes. The $H\gamma\gamma$ coupling has a destructive interference term arising from the contributions from fermion loops and the W-boson loop that introduces a term linear in κ_W and κ_f. This term breaks the ambiguity of the relative sign between κ_W and κ_f, although the contribution from the $H \to \gamma\gamma$ channels is weak in the analyses presented here. A smaller interference term exists in the ggH coupling, in which the dominant fermion-loop contributions interfere constructively with two-loop electroweak contributions [30,38]. A

global sign on all Higgs boson couplings is unobservable in the current analysis.

We study each coupling scale factor independently, holding the others fixed to their SM values, and then to study the fits by relaxing the assumptions one at a time. We first study κ_W, setting $\kappa_f = \kappa_Z = 1$. The posterior probability distribution for κ_W is shown in Fig. 13. The factor κ_W is constrained to the intervals $-1.8 < \kappa_W < -0.8$ and $1.0 < \kappa_W < 1.7$ at the 68% C.L. The best fit value for κ_W is -1.4. We perform a similar fit for κ_Z, setting $\kappa_f = \kappa_W = 1$. From the posterior probability distribution shown in Fig. 14, κ_Z is constrained at the 68% C.L. to the intervals $-1.5 < \kappa_Z < -0.4$ and $0.4 < \kappa_Z < 1.5$. The best fit value for κ_Z is 1.05. We also perform a one-dimensional fit for the Higgs boson coupling to fermions, κ_f, setting $\kappa_W = \kappa_Z = 1$. The posterior probability distribution obtained from the fit is shown in Fig. 15. In this case κ_f is restricted at the 68% C.L. to the intervals $-3.8 < \kappa_f < -1.2$ and $2.0 < \kappa_f < 3.0$ and has a best fit value of -2.75.

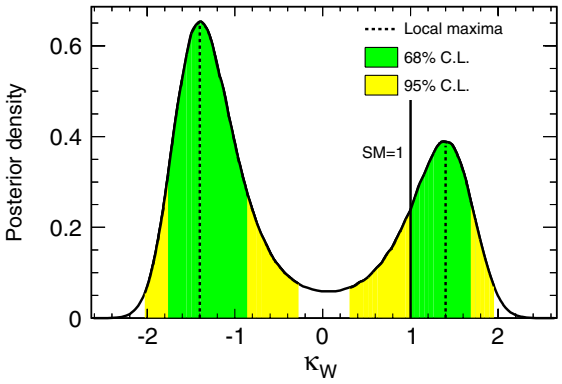

FIG. 13 (color online). Posterior probability distribution for κ_W from the combination of all CDF search channels. In performing this fit, the values for κ_Z and κ_f are fixed to their SM values ($\kappa_Z = \kappa_f = 1$).

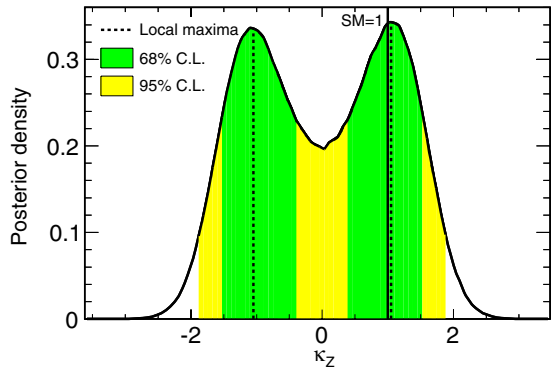

FIG. 14 (color online). Posterior probability distribution for κ_Z from the combination of all CDF search channels. In performing this fit, the values for κ_W and κ_f are fixed to their SM values ($\kappa_W = \kappa_f = 1$).

We also constrain the allowed parameter space in the two-dimensional (κ_W, κ_Z) plane. A fit to the observed data is performed allowing all three coupling parameters to float. Two-dimensional constraints on (κ_W, κ_Z) are obtained from the resulting three-dimensional posterior probability distribution by integrating over κ_f. The smallest regions containing 68% and 95% of the integral of the posterior probability density are shown in Fig. 16. As a result of the global sign ambiguity in the couplings, the value of the posterior probability at $(-\kappa_W, \kappa_Z)$ is equal to

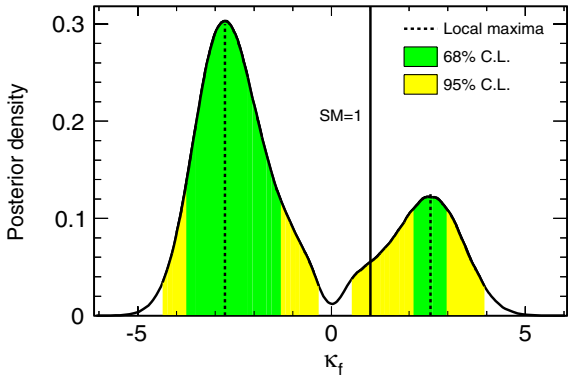

FIG. 15 (color online). Posterior probability distribution for κ_f from the combination of all CDF search channels. In performing this fit, the values for κ_W and κ_Z are fixed to their SM values ($\kappa_W = \kappa_Z = 1$).

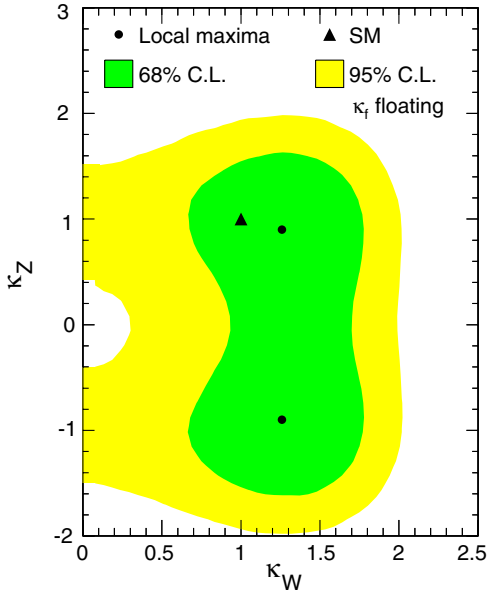

FIG. 16 (color online). Two-dimensional constraints in the (κ_W, κ_Z) plane. The 68% and 95% credibility regions are shown. A three-dimensional posterior probability distribution is obtained from a fit to the observed data in all CDF search channels by floating all three coupling parameters (κ_W, κ_Z, and κ_f). The two-dimensional constraints are obtained by integrating the three-dimensional posterior probability density over κ_f.

the value at $(\kappa_W, -\kappa_Z)$. Similarly, the value of the posterior probability at $(-\kappa_W, -\kappa_Z)$ is equal to the value at (κ_W, κ_Z). The posterior probability distribution in Fig. 16 is displayed only for positive values of κ_W. The local maxima within the regions of positive and negative κ_Z are $(\kappa_W = 1.3,\ \kappa_Z = 0.9)$ and $(\kappa_W = 1.3,\ \kappa_Z = -0.9)$, respectively.

Finally, we constrain the allowed parameter space within the two-dimensional (κ_V, κ_f) plane. Here, κ_V refers to a generic coupling of the Higgs boson to both W and Z bosons where the ratio $\lambda_{WZ} = \kappa_W/\kappa_Z$ is fixed to unity. We compute a two-dimensional posterior probability distribution in the (κ_V, κ_f) plane assuming a uniform prior probability density. The smallest regions containing 68% and 95% of the integral of the posterior probability density are shown in Fig. 17. Accounting for the symmetries $(-\kappa_V, \kappa_f) = (\kappa_V, -\kappa_f)$ and $(-\kappa_V, -\kappa_f) = (\kappa_V, \kappa_f)$ the posterior probability distribution is only displayed for positive values of κ_V. The local maxima within the regions of positive and negative κ_f are $(\kappa_V = 1.05, \kappa_f = 2.6)$ and $(\kappa_V = 1.05, \kappa_f = -2.7)$.

The results in the (κ_V, κ_f) plane shown here are more constraining than those previously extracted in Ref. [101]. This is due to the inclusion of more channels and the use of separate scalings for each signal component, itemized by production and decay mode, contributing to individual search channels. The search channels with the most sensitivity to SM Higgs boson production measure the product of vector boson and fermion couplings. For example,

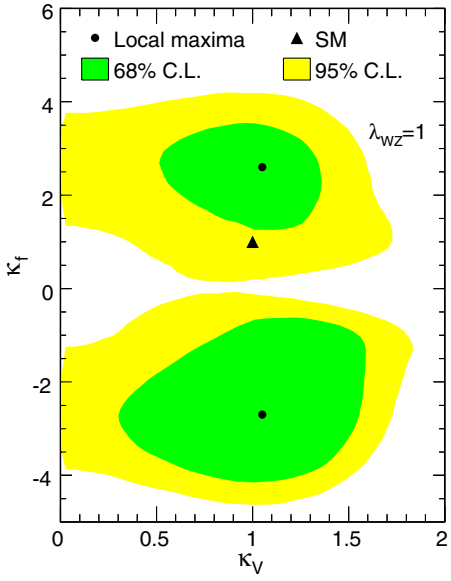

FIG. 17 (color online). Two-dimensional constraints in the (κ_V, κ_f) plane. The 68% and 95% credibility regions are shown. A two-dimensional posterior probability distribution is obtained from a fit to the observed data in all CDF search channels where κ_V is the generic Higgs boson coupling to W and Z bosons assuming the SM value of one for $\lambda_{WZ} = \kappa_W/\kappa_Z$.

search modes focusing on decays to fermion pairs ($b\bar{b}$ and $\tau^+\tau^-$) require production in association with a vector boson. Conversely, searches focusing on Higgs boson decays to W^+W^- and ZZ pairs obtain a majority of their sensitivity from $gg \to H$ production, which proceeds mostly via fermionic couplings to the Higgs boson. Our searches for $t\bar{t}H \to t\bar{t}b\bar{b}$, on the other hand, are sensitive primarily to κ_f in both the production and decay modes. Hence, this search channel contributes significantly to the observed constraints on the coupling parameters, although it provides only a small contribution to combined CDF SM search result. Similarly, search channels focusing on events with same-charge dileptons and trileptons are sensitive to κ_V in both the production (VH) and decay ($H \to W^+W^-$) modes. These channels provide a loose constraint on κ_V independent of κ_f and in the process help eliminate tails in the posterior probability distributions.

XI. SUMMARY

In summary, we present a final combination of the CDF Higgs boson searches. In the context of the standard model, we exclude at the 95% C.L. Higgs bosons with masses in the ranges $90 < m_H < 102$ GeV/c^2 and $149 < m_H < 172$ GeV/c^2. In the absence of a signal, we expect to exclude the ranges $90 < m_H < 94$ GeV/c^2, $96 < m_H < 106$ GeV/c^2, and $153 < m_H < 175$ GeV/c^2. An excess of data with respect to background predictions is observed, which has a local significance of 2.0 standard deviations at $m_H = 125$ GeV/c^2. We exclude fermiophobic Higgs boson bosons with mass in the range $100 < m_H < 113$ GeV/c^2 and expect to exclude $100 < m_H < 122$ GeV/c^2 in the absence of a Higgs boson signal. In the fourth-generation scenario incorporating the lowest possible fourth-generation lepton and neutrino masses, we exclude the range $124 < m_H < 203$ GeV/c^2 at the 95% C.L. and expect to exclude $123 < m_H < 231$ GeV/c^2. The constraints placed on the fermionic and bosonic couplings are consistent with standard model expectations.

ACKNOWLEDGMENTS

We would like to thank the authors of the HAWK program for adapting it to the Tevatron. We thank the Fermilab staff and the technical staffs of the participating institutions for their vital contributions. This work was supported by the U.S. Department of Energy and National Science Foundation; the Italian Istituto Nazionale di Fisica Nucleare; the Ministry of Education, Culture, Sports, Science and Technology of Japan; the Natural Sciences and Engineering Research Council of Canada; the National Science Council of the Republic of China; the Swiss National Science Foundation; the A. P. Sloan Foundation; the Bundesministerium für Bildung und Forschung, Germany; the Korean World Class University Program,

the National Research Foundation of Korea; the Science and Technology Facilities Council and the Royal Society, United Kingdom; the Russian Foundation for Basic Research; the Ministerio de Ciencia e Innovación, and Programa Consolider-Ingenio 2010, Spain; the Slovak R&D Agency; the Academy of Finland; the Australian Research Council (ARC); and the EU community Marie Curie Fellowship Contract No. 302103.

[1] S. L. Glashow, Nucl. Phys. **22**, 579 (1961); S. Weinberg, Phys. Rev. Lett. **19**, 1264 (1967); A. Salam, in *Elementary Particle Theory*, edited by N. Svartholm (Almqvist & Wiksell, Stockholm, 1968), p. 367.

[2] F. Englert and R. Brout, Phys. Rev. Lett. **13**, 321 (1964); P. W. Higgs, Phys. Rev. Lett. **13**, 508 (1964); G. S. Guralnik, C. R. Hagen, and T. W. B. Kibble, Phys. Rev. Lett. **13**, 585 (1964); P. W. Higgs, Phys. Rev. **145**, 1156 (1966).

[3] ALEPH, CDF, D0, DELPHI, L3, OPAL, and SLD Collaborations, LEP Electroweak Working Group, Tevatron Electroweak Working Group, and SLD Electroweak and Heavy Flavour Working Groups, arXiv:1012.2367.

[4] CDF and D0 Collaborations and Tevatron Electroweak Working Group, arXiv:1204.0042.

[5] T. Aaltonen *et al.* (CDF and D0 Collaborations), Phys. Rev. D **86**, 092003 (2012).

[6] ALEPH, DELPHI, L3 and OPAL Collaborations, and LEP Working Group for Higgs Boson Searches, Phys. Lett. B **565**, 61 (2003).

[7] G. Aad *et al.* (ATLAS Collaboration), Phys. Lett. B **716**, 1 (2012).

[8] S. Chatrchyan *et al.* (CMS Collaboration), Phys. Lett. B **716**, 30 (2012).

[9] Here, and throughout the paper, charge conjugate states are implied. The label ℓ indicates an electron or a muon but not a tau lepton. Flavor indices on neutrinos are also implied. $W^- \to \ell^- \bar{\nu}_\ell$ is written $W \to \ell\nu$.

[10] T. Aaltonen *et al.* (CDF Collaboration and D0 Collaboration), Phys. Rev. Lett. **109**, 071804 (2012).

[11] A. Akeroyd, Phys. Lett. B **368**, 89 (1996).

[12] H. Haber, G. L. Kane, and T. Sterling, Nucl. Phys. **B161**, 493 (1979).

[13] H. Pois, T. J. Weiler, and T. C. Yuan, Phys. Rev. D **47**, 3886 (1993).

[14] A. G. Akeroyd and M. A. Diaz, Phys. Rev. D **67**, 095007 (2003).

[15] G. D. Kribs, T. Plehn, M. Spannowsky, and T. M. Tait, Phys. Rev. D **76**, 075016 (2007).

[16] A. Denner, S. Dittmaier, A. Mück, G. Passarino, M. Spira, C. Strum, S. Uccirati, and M. Weber, Eur. Phys. J. C **72**, 1992 (2012).

[17] C. Anastasiou, R. Boughezal, and E. Furlan, J. High Energy Phys. 06 (2010) 101.

[18] D. Acosta *et al.* (CDF Collaboration), Phys. Rev. D **71**, 052003 (2005).

[19] D. Acosta *et al.* (CDF Collaboration), Phys. Rev. D **71**, 032001 (2005); A. Abulencia *et al.* (CDF Collaboration), J. Phys. G **34**, 2457 (2007).

[20] C. S. Hill, Nucl. Instrum. Methods Phys. Res., Sect. A **511**, 118 (2003); A. Sill *et al.*, Nucl. Instrum. Methods Phys. Res., Sect. A **447**, 1 (2000); A. Affolder *et al.*, Nucl. Instrum. Methods Phys. Res., Sect. A **453**, 84 (2000).

[21] We use a cylindrical coordinate system with origin in the center of the detector where θ and ϕ are the polar and azimuthal angles, respectively, and pseudorapidity is $\eta = -\ln\tan(\theta/2)$. The missing E_T ($\not\!\!E_T$) is defined by $\not\!\!E_T = -\sum_i E_T^i \hat{n}_i$, i = calorimeter tower number, where $\hat{n}_i$ is a unit vector perpendicular to the beam axis and pointing at the ith calorimeter tower. The calculation for $\not\!\!E_T$ includes jet-energy correction and corrections for high-energy muons. We define $\not\!\!E_T = |\vec{\not\!\!E}_T|$. The transverse momentum p_T is defined to be $p\sin\theta$.

[22] G. Ascoli, L. E. Holloway, I. Karliner, U. E. Kruse, R. D. Sard, V. J. Simaitis, D. A. Smith, and T. K. Westhusing, Nucl. Instrum. Methods Phys. Res., Sect. A **268**, 33 (1988).

[23] D. Acosta *et al.*, Nucl. Instrum. Methods Phys. Res., Sect. A **494**, 57 (2002).

[24] S. Klimenko, J. Konigsberg, and T. M. Liss, Report No. FERMILAB-FN-0741, 2003.

[25] E. J. Thomson *et al.*, IEEE Trans. Nucl. Sci. **49**, 1063 (2002).

[26] G. Gomez-Ceballos *et al.*, Nucl. Instrum. Methods Phys. Res., Sect. A **518**, 522 (2004).

[27] A. Bhatti *et al.*, Nucl. Instrum. Methods Phys. Res., Sect. A **566**, 375 (2006).

[28] T. Sjostrand, S. Mrenna, and P. Skands, J. High Energy Phys. 05 (2006) 026. We use PYTHIA version 6.216 to generate the Higgs boson signals.

[29] H. L. Lai, J. Huston, S. Kuhlmann, J. Morfin, F. Olness, J. F. Owens, J. Pumplin, and W. K. Tung, Eur. Phys. J. C **12**, 375 (2000); J. Pumplin, D. R. Stump, J. Huston, H-L. Lai, P. Nadolsky, and W-K. Tung, J. High Energy Phys. 07 (2002) 012.

[30] C. Anastasiou, R. Boughezal, and F. Petriello, J. High Energy Phys. 04 (2009) 003.

[31] D. de Florian and M. Grazzini, Phys. Lett. B **674**, 291 (2009).

[32] M. Grazzini (private communication).

[33] A. D. Martin, W. J. Stirling, R. S. Thorne, and G. Watt, Eur. Phys. J. C **63**, 189 (2009).

[34] M. Botje *et al.*, arXiv:1101.0538.

[35] R. V. Harlander and W. B. Kilgore, Phys. Rev. Lett. **88**, 201801 (2002).

[36] C. Anastasiou and K. Melnikov, Nucl. Phys. **B646**, 220 (2002).

[37] V. Ravindran, J. Smith, and W. L. van Neerven, Nucl. Phys. **B665**, 325 (2003).

[38] S. Actis, G. Passarino, C. Sturm, and S. Uccirati, Phys. Lett. B **670**, 12 (2008).
[39] U. Aglietti, R. Bonciani, G. Degrassi, and A. Vicini, arXiv:hep-ph/0610033.
[40] S. Catani, D. de Florian, M. Grazzini, and P. Nason, J. High Energy Phys. 07 (2003) 028.
[41] T. Aaltonen *et al.* (CDF Collaboration), Phys. Rev. Lett. **109**, 111804 (2012).
[42] T. Aaltonen *et al.* (CDF Collaboration), Phys. Rev. D **87**, 052008 (2013).
[43] T. Aaltonen *et al.* (CDF Collaboration), Phys. Rev. Lett. **109**, 111803 (2012).
[44] T. Aaltonen *et al.* (CDF Collaboration), Report No. FERMILAB-PUB-13-029-E.
[45] T. Aaltonen *et al.* (CDF Collaboration), Phys. Rev. D **86**, 072012 (2012).
[46] T. Aaltonen *et al.* (CDF Collaboration), Phys. Rev. Lett. **108**, 181804 (2012).
[47] T. Aaltonen *et al.* (CDF Collaboration), J. High Energy Phys. 02 (2013) 004.
[48] T. Aaltonen *et al.* (CDF Collaboration), Phys. Lett. B **717**, 173 (2012).
[49] T. Aaltonen *et al.* (CDF Collaboration), Phys. Rev. Lett. **109**, 181802 (2012).
[50] I. W. Stewart and F. J. Tackmann, Phys. Rev. D **85**, 034011 (2012).
[51] S. Dittmaier *et al.* (LHC Higgs Cross Section Working Group), arXiv:1201.3084.
[52] C. Anastasiou, G. Dissertori, M. Massimiliano, F. Stockli, and B. Webber, J. High Energy Phys. 08 (2009) 099.
[53] J. M. Campbell, R. K. Ellis, and C. Williams, Phys. Rev. D **81**, 074023 (2010).
[54] G. Bozzi, S. Catani, D. de Florian, and M. Grazzini, Phys. Lett. B **564**, 65 (2003); Nucl. Phys. **B737**, 73 (2006).
[55] C. Balazs, J. Huston, and I. Puljak, Phys. Rev. D **63**, 014021 (2000); C. Balazs and C.-P. Yuan, Phys. Lett. B **478**, 192 (2000); Qing-Hong Cao and Chuan-Ren Chen, Phys. Rev. D **76**, 073006 (2007).
[56] J. Baglio and A. Djouadi, J. High Energy Phys. 10 (2010) 064.
[57] The FORTRAN program can be found on http://people.web.psi.ch/~mspira/proglist.html.
[58] O. Brein, A. Djouadi, and R. Harlander, Phys. Lett. B **579**, 149 (2004).
[59] M. L. Ciccolini, S. Dittmaier, and M. Kramer, Phys. Rev. D **68**, 073003 (2003).
[60] G. Ferrera, M. Grazzini, and F. Tramontano, Phys. Rev. Lett. **107**, 152003 (2011).
[61] P. Bolzoni, F. Maltoni, S.-O. Moch, and M. Zaro, Phys. Rev. Lett. **105**, 011801 (2010).
[62] M. Ciccolini, A. Denner, and S. Dittmaier, Phys. Rev. Lett. **99**, 161803 (2007); Phys. Rev. D **77**, 013002 (2008).
[63] W. Beenaker, S. Dittmaier, M. Kramer, B. Plumper, M. Spira, and P. M. Zerwas, Phys. Rev. Lett. **87**, 201805 (2001); L. Reina and S. Dawson, Phys. Rev. Lett. **87**, 201804 (2001).
[64] S. Dittmaier *et al.* (LHC Higgs Cross Section Working Group), arXiv:1101.0593.
[65] A. Djouadi, J. Kalinowski, and M. Spira, Comput. Phys. Commun. **108**, 56 (1998).
[66] A. Bredenstein, A. Denner, S. Dittmaier, and M. M. Weber, Phys. Rev. D **74**, 013004 (2006); A. Bredenstein, A. Denner, S. Dittmaier, A. Mück, and M. M. Weber, J. High Energy Phys. 02 (2007) 080.
[67] J. Baglio and A. Djouadi, J. High Energy Phys. 03 (2011) 055.
[68] A. Denner, S. Heinemeyer, I. Puljak, D. Rebuzzi, and M. Spira, Eur. Phys. J. C **71**, 1753 (2011).
[69] J. Freeman, T. Junk, M. Kirby, Y. Oksuzian, T. J. Phillips, F. D. Snider, M. Trovato, J. Vizan, and W. M. Yao, Nucl. Instrum. Methods Phys. Res., Sect. A **697**, 64 (2013).
[70] A. Abulencia *et al.* (CDF Collaboration), Phys. Rev. D **74**, 072006 (2006).
[71] T. Aaltonen, A. Buzatu, B. Kilminster, Y. Nagai, and W. Yao, arXiv:1107.3026.
[72] T. Aaltonen *et al.* (CDF Collaboration), Phys. Lett. B **715**, 98 (2012).
[73] T. Aaltonen *et al.* (CDF Collaboration), Phys. Rev. D **85**, 072001 (2012).
[74] T. Aaltonen *et al.* (CDF Collaboration), Phys. Rev. D **86**, 032011 (2012).
[75] T. Aaltonen *et al.* (CDF Collaboration), Phys. Rev. Lett. **109**, 111805 (2012).
[76] B. S. Park, Ph.D. thesis, [Ohio State University, Report No. FERMILAB-THESIS-2008-18].
[77] J. M. Campbell and R. K. Ellis, Phys. Rev. D **60**, 113006 (1999).
[78] S. Moch and P. Uwer, Nucl. Phys. B, Proc. Suppl. **183**, 75 (2008).
[79] N. Kidonakis, Phys. Rev. D **74**, 114012 (2006).
[80] T. Aaltonen *et al.* (CDF Collaboration), Phys. Rev. Lett. **103**, 092002 (2009).
[81] T. Aaltonen *et al.* (CDF Collaboration), Phys. Rev. D **82**, 112005 (2010).
[82] T. Aaltonen *et al.* (CDF Collaboration), Phys. Rev. D **81**, 072003 (2010).
[83] T. Aaltonen *et al.* (CDF Collaboration), Phys. Rev. Lett. **104**, 201801 (2010).
[84] T. Aaltonen *et al.* (CDF Collaboration), Phys. Rev. Lett. **108**, 101801 (2012).
[85] D. Acosta *et al.*, Phys. Rev. D **86**, 031104(R) (2012).
[86] See Supplemental Material at http://link.aps.org/supplemental/10.1103/PhysRevD.88.052013 for alternative versions of Figs. 1 and 2.
[87] G. Aad *et al.* (ATLAS Collaboration), Phys. Rev. D **86**, 032003 (2012).
[88] S. Chatrchyan *et al.* (CMS Collaboration), Phys. Lett. B **710**, 26 (2012).
[89] T. Aaltonen *et al.* (CDF and D0 Collaborations), arXiv:1109.0576.
[90] V. M. Abazov *et al.* (D0 Collaboration), Phys. Rev. Lett. **102**, 231801 (2009).
[91] T. Aaltonen *et al.* (CDF Collaboration), Phys. Rev. Lett. **103**, 061803 (2009).
[92] G. Aad *et al.* (ATLAS Collaboration), Eur. Phys. J. C **72**, 2157 (2012).
[93] S. Chatrchyan *et al.* (CMS Collaboration), J. High Energy Phys. 09 (2012) 111.
[94] T. Aaltonen *et al.* (CDF and D0 Collaborations), Phys. Rev. D **82**, 011102 (2010).

[95] G. Aad *et al.* (ATLAS Collaboration), Eur. Phys. J. C **71**, 1728 (2011).
[96] S. Chatrchyan *et al.* (CMS Collaboration), Phys. Lett. B **699**, 25 (2011).
[97] S. Chatrchyan *et al.* (CMS Collaboration), arXiv:1302.1764.
[98] S. Chatrchyan *et al.* (CMS Collaboration), Report No. CMS-PAS-HIG-12-020, 2012.
[99] G. Aad *et al.* (ATLAS Collaboration), Report No. ATLAS-CONF-2012-127, 2012.
[100] A. David, A. Denner, M. Duehrssen, M. Grazzini, C. Grojean, G. Passarino, M. Schumacher, M. Spira, G. Weiglein, and M. Zanettind (LHC Higgs Cross Section Working Group), arXiv:1209.0040.
[101] J. Espinosa, C. Grojean, M. Muhlleitner, and M. Trott, J. High Energy Phys. 12 (2012) 045.